Large Eddy Simulation On Vortex Shedding For A Helical-Twisted Cylinder Subjected To Crossflow

Sergio Mohr Peraza

A thesis presented for the Master degree of
MSc in Sustainable Energy Engineering:
Process Engineering and Combustion Technology

Department of Energy Technology
Aalborg University
June 16, 2020

Department Of Energy Technology
Aalborg University
http://www.aau.dk

AALBORG UNIVERSITY

Title:
Large Eddy Simulation On Vortex Shedding For A Helical-Twisted Cylinder Subjected To Crossflow

Master's Thesis Period:
Spring Semester 2020

Author:
Sergio Mohr Peraza

Supervisor:
Matthias Mandø

Company collaboration with:
AcuRail

Page Count (excl. blanks): 33

Date of Completion:
June 16, 2020

Keywords:
Helical-twisted cylinder
LES turbulence model
Vortex shedding
Aerodynamic forces
Vortex-induced vibrations

Abstract:

Helical-twisted cylinders are used in safety applications. Due to its imperfect cross-section a better grip is achieved. In this Master thesis, a LES turbulence model is made to predict the behavior of vortex shedding on helical-twisted profiles. A numerical model for a circular cylinder is investigated and compared to several configurations of the groove's height (e) and pitch (p). This comparison is carried out in order to find the design in which the suppression of vortex-induced vibrations is optimized. Simulations are done by subjecting the body of six different cylinders to an air crossflow, with a Reynolds number of $3.7 \cdot 10^4$. The aerodynamic force coefficients are also recorded for the evaluation of the vortex shedding reduction mechanism. It is found that the helical-twisted profile with p/D = 1 and e/D = 0.05 effectively mitigate the vortex shedding frequency by 16%, in comparison to the circular cylinder. This is related to the damping of the fluctuating lift forces and their spanwise correlation. Therefore, improvements in the three-dimensional disturbance by the near wall wake are achieved. With regard to the other helical-twisted pipe configurations, they are proven to be insufficient for this matter, thus concluding that deeper or larger cavities can lead to an exacerbation of the vortex shedding phenomena. Nevertheless, damping of the lift force amplitude fluctuations is achieved for the cases of p/D = 1 e/D = 0.2, p/D = 2 e/D = 0.1 and p/D = 0.5 e/D = 0.1.

Nomenclature

Symbol	Description	Unit
A	Area	m^2
C_D	Drag coefficient	-
C_f	Skin friction coefficient	-
C_k	Kolmogrov constant	-
C_L	Lift coefficient	-
C_s	Smagorinsky constant	-
Co	Courant number	-
D	Diameter	m
F_D	Drag force	N
F_L	Lift lift	N
f	Shedding frequency	Hz
L	Length	m
L_S	Mixing length for subgrid scales	-
U	Freestream velocity	m s^{-1}
$\bar{u}$	Filtered velocity	m s^{-1}
u^*	Friction velocity	m s^{-1}
$\bar{p}$	Filtered pressure	Pa
Re_D	Reynolds number	-
Sr	Strouhal number	-
$\bar{S}_{ij}$	Rate-of-strain tensor	s^{-1}
t	Time	s
y^+	Dimensionless wall distance for a wall-bounded flow	-

Greek symbol	**Description**	Unit
ρ	Density	kg m^{-3}
μ	Dynamic viscosity	kg m^{-1} s^{-1}
μ_t	Subgrid-scale turbulent viscosity	kg m^{-1} s^{-1}
ν	Kinematic viscosity	m^{2} s^{-1}
τ_{ij}	Subgride-scale stress	Pa
τ_w	Wall-shear stress	Pa

Acronyms	**Description**
CFD	Computational Fluid Dynamics
DNS	Direct Numerical Simulation
FFT	Fast Fourier Transformation
FSI	Fluid-Structure Interaction
LES	Large Eddy Simulation
PSD	Power Spectral Density
RANS	Reynolds-Averaged Navier-Stokes
SGS	Subgrid-scale
VIV	Vortex-Induced Vibrations

Contents

Preface

This Master thesis was made by Sergio Mohr Peraza, at Aalborg University Esbjerg. The thesis has been carried out in the period from February 2020 to June 2020, corresponding to the 4^{th} Semester. The project has been offered to the student through a collaboration with the company AcuRail, which has a total of 10 staff members. The offices are located in Esbjerg, Denmark. AcuRail is the main distributor of KAG Safety Rail in Denmark and are currently exploring new applications for their helical-twisted rail product. Hence, the development of this document.

Throughout the project period, the author made use of empirical data from experiments supplied by the company. In that regard, the student would like to thank Torben H. Pedersen, CEO of the company, for offering this research opportunity and his useful information about the product subjected to analysis. As well as to Associate Professor Matthias Mandø, not only for his guidance and support during the project development, but also for being the link between the academical institution and the company.

Aalborg University, June 16, 2020

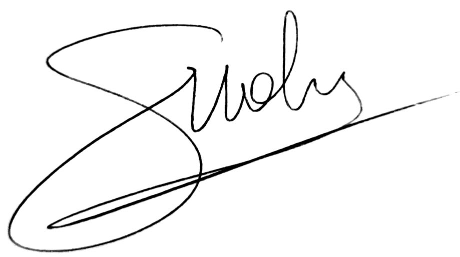

Sergio Mohr Peraza
smohrp18@student.aau.dk

Chapter 1

Introduction

Circular pipes are frequently chosen as a solution for different industrial applications, due to their simplicity in the manufacturing procedure and cost-effectiveness. In the cylinders, it is also common to employ materials that give smoothness to the surface, such as aluminium or stainless steel. There is a wide variety of designs depending on the final usage, where specific features (such as safety) should be considered and optimized. Due to the circular shape and the smoothness involved, when the material gets covered by water or oily substances, it turns into a slippery surface with a potential danger for the user. This situation can be seen in circumstances where the cylinder is employed as a support structure, like pipes in a household's shower or risky environments in offshore facilities.

Helical-twisted or sinusoidally corrugated cylindrical profile is a solution given by KAG Safety Rail, from which AcuRail is the main european distributor. The proposed geometry gives an imperfect circular cross-section that allows the user to adapt the hand around for a better griping. An example of the pipe is shown in Figure 1.1.

Figure 1.1: **Helical-twisted pipe profile solution by AcuRail [1]**

The profile has been tested by Queensland University of Technology (QUT) under standard grip performance conditions. In these experiments, the product has been proven to increase grip up to 80% under wet conditions, up to 160% in dry conditions and to 300% in oily conditions in comparison to standard marketable grab rail [2]. Therefore, the spirally corrugated pipe has a long list of possible implementations involving safety improving: scaffolding, industry, offshore facilities, public areas, elder care and ships.

Currently, the company has been exploring the application of such profile in the construction of lattice towers. These type of structures are often made by circular cylinder profiles, whose design is regularly associated with uncontrolled movements owing to vortex shedding. This interaction create numerous oscillations in the weld joints of the structure, which compromises its integrity with failure risk. In Appendix A, a report made by NordBase for AcuRail shows, in which they assessed the suitability of the helical-twisted cylinder to lattice towers. Based on that, they concluded that it its interesting to develop a model which may predict if the profile could remedy the structural issues by vortex damping.

When an immersed bluff body, a cylinder in this case, is subjected to a crossflow, the fluid reduces its velocity at the surface due to viscosity forces, thus giving the boundary layer. Subsequently, the boundary layer encounters an adverse pressure gradient, given by the curvature of the body and separates from the surface. Therefore, vortices are created downstream close to the wall. At some point, the stability of the vortices is compromised and eventually detached. Thereby, unsteady flow separation takes place and the wake sheds intermittently periodic vortices at opposite upstream sides, hence vortex shedding. The repeating pattern of these swirling vortices is known by the name of Kármán vortex street [3], see Figure 1.2.

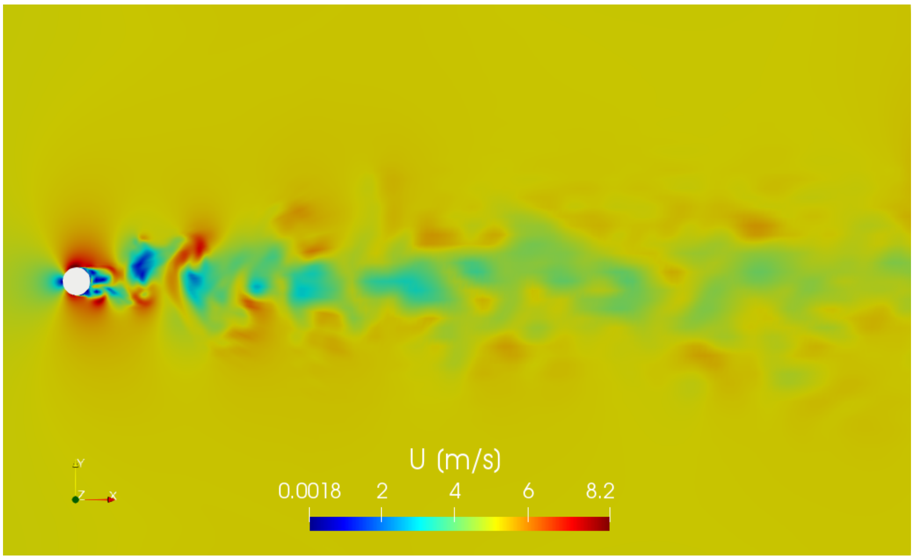

Figure 1.2: **Velocity contour on vortex shedding of a circular cylinder with D = 114 mm subjected to air crossflow at Re = $3.7 \cdot 10^4$**

This asymmetric formation of vortices cause an alternating low-pressure region in the downstream side of the structure, near the wall. It subjects the cylinder to fluctuating forces, transverse to the flow direction. Those oscillations can put the structure in motion following a periodic pattern. The described interaction is known as vortex-induced vibrations (VIV).

VIV is a typical fluid-structure interaction (FSI) that occurs in numerous engineering fields: renewable energy, marine, wind, etc. Thus, it has become in a capital subject of analysis [4]. If the frequency of the VIV reaches values close to the natural frequency of the body, the phenomena of resonance takes place, also known as "lock-in". Thereby, the integrity of the structure is compromised and the time to failure of the material by fatigue damage is accelerated. In the long run, this can be translated in expenses related to both maintenance and replacement costs [5].

The difficulty of the excitation prediction relies on several features like the Reynolds number or the degree of flow turbulence. The Reynolds number is a contrasted parameter to have a major influence in the degree of either VIV and vortex shedding [6]. However, there are three of them that rise among the factors and have an important effect on the degree of VIV instability: surface roughness, flow angle of attack and cross sectional shape [7]. These features can be controlled in an experimental and numerical way for prediction and measure. *Gao et al.* [8] found in their research that cylinders with rough surfaces have a smaller VIV displacement, thus narrowing the lock-in region in comparison to a smooth-surface cylinder, decreasing the lift and drag forces. Regarding the vortex shedding frequency, not significant changes were encountered at increasing degrees of surface roughness. When it comes to the flow incidence, *Zhao et al.* [9] stated that for a squared cylinder the body oscillation amplitude can change for different angles, even getting to the point of reducing the vortex-induced vibrations. At the same time, this effect exposes the importance of the cross sectional shape in the outcome of the oscillations and vortex shedding, because the geometry influences the direction of the flow downstream and the level of the generated pressure gradients. *Carlson et al.* [10] studied the influence of different geometries in the degree of VIV.

Over the last decades, different experiments have been carried out in order to measure the vortex shedding behind a rigid circular cylinder immersed with a cross-directional flow for many engineering applications. Researchers like *Feng* first focused on elastically mounted cylinder with an incoming air flow in order to measure the resonance [11]. Wind Engineering and the industrial aerodynamics have a big interest in this kind of studies.

Furthermore, studies also turned its eyes towards water crossing flows in the marine engineering [12], where density is generally a thousand times higher than air. In these scenarios, VIV happen for a much wider regime of low-velocities, whereas the possible frequencies of response are different compared to when air is considered [5]. Studies that compare the impact of both, fluid in the fluid-structure interaction with similar configurations, started a long time ago. For instance, *Vickery and Watkins* stated in the first Australasian conference of 1962 that helical strakes surrounding the surface of the cylinder were as effective in the water as if it is subjected to air [13].

Different methods were developed in order to counteract the excitation from vortex-induced vibration: surface protrusions, shrouds and near-wake stabilisers [14], see Figure 1.3. The usage of fitted helical strakes is a surface protrusion countermeasure, which is widely admitted to increase the stability and decrease the fatigue in the body by affecting the separation lines or shear layers [5]. *Ranjith et al.* comes to the conclusion that this reduces the value of VIV generation up to 99% [15]. Helical wires of rounded section may be considered to be a great alternative to helical strakes due to its equivalence in the performance. As a matter of fact, this variant in the design may reduce the drag and lift coefficient since the surface material is less sharp than a strake geometry in the edge of a cylinder [16]. Regarding this, *Ishibara et al.* comes to the conclusion that the lock-in can be avoided for any freestream velocity with rounded wires of 0.1 in d/D ratio, reducing the resulting lift force, even though the drag force remains unaltered.

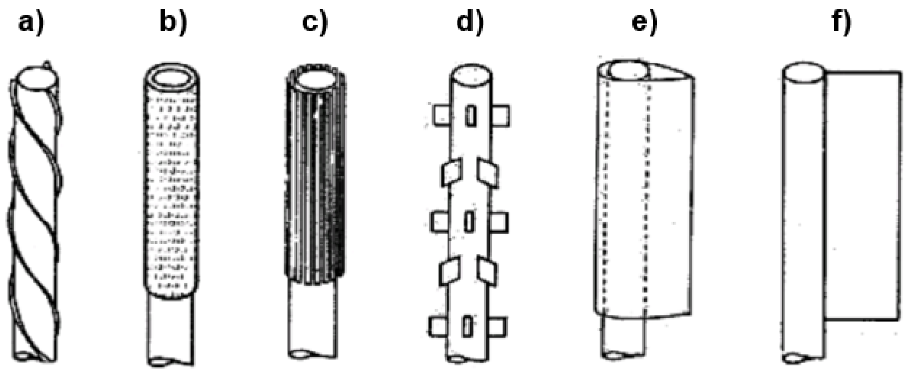

Figure 1.3: **Example of different vortex shedding countermeasures: a) helical strakes, b) shroud, c) axial slats, d) spoiler plates, e) streamlined fairing and f) splitter [3]**

There is a wide palette of numerical studies on the vortex shedding and its induced vibrations for simple geometries, such as a circular cylinder. However, to the best of the authors knowledge, there is a lack of numerical studies on spirally corrugated pipes, as well as on other combinations in the design with similar complexity in the geometry. This suggest that the field may not be fully developed. Therefore the mechanical features of the profile in the fluid-structure interface may not be fully understood yet. Instead, thermal numerical approaches have been carried out by researchers regarding this matter in order to enhance the energy transmission between fluid and environment. For instance, *Ganeshan et al.* [17] studied experimentally a circular cylinder and compared it to seven different spirally corrugated cylinders. Subsequently, they come to the conclusion that the twisting geometry enhances the heat exchanging capacity up to a 100% more than a simpler circular tube. Furthermore, *Sørensen et al.* [18] numerically assessed the effects of the spirally corrugated cylinder with 28 different geometry degrees of groove's pith and height, where the results show the patterns to give a significant heat-transfer enhancing in the flow characteristics.

The three-dimensionality is often neglected in vortex shedding modelling. This approach seems to be insufficient, because from very low Reynolds number the flow in the wake becomes three-dimensional in spite of applicable time-averaged parameters. As discussed by *Williamson* [19] in his research about the existence of this transition from two to three-dimensional fluid, with Reynolds number of around 200 the fluctuations are not correlated along the span of the body.

This is why three-dimensional turbulence models of Computational Fluid Dynamics (CFD) are currently carried out to measure lock-in issues and the deflection that takes place [20], but still so far helical-twisted pipes are not an object of study. Although, this profile does not exactly match with the geometry of the mentioned wires, they can lead the way in the study of how the twisted tube operate under VIV conditions.

Hence, numerical simulations of FSI becomes important in order to investigate the mentioned mechanisms, by coupling the unsteady flow in the wake patterns with the resulting lift and drag forces and the dynamic response of the structure.

In this Master thesis, a numerical simulation on the vortex-shedding is carried out, by using Large Eddy Simulation (LES) turbulence model for a total of six different cylinders. Here, a circular cylinder and five different sinusoidal corrugated cylinders are tested and compared with different groove's height and length designs. By using a well-known open source program called OpenFOAM, simulations are run in order to calculate the resultant unsteady turbulent flow generated immediately upstream from they body, thus giving the contours of filtered pressure, velocity magnitude and the calculated aerodynamic force coefficients of drag and lift. The latter dimensionless number immediately gives the vortex shedding frequency, which lately enables the calculation of the Strouhal number.

The vortex shedding on a circular cylinder subjected to a crossflow is a well-known study field, as well as, a wide variety of different mechanism design is the main attraction in order to mitigate the phenomena as much as possible. Helical-twisted cylinders are profiles with successful use in the safety industry due to its better grip capacity, besides showing potential for further applications as the vortex shedding suppression. Since its shape bears resemblance with a mitigation mechanism as the helical strakes. In addition, it has been proven to be an interesting alternative for lattice towers, where the reduction of vortex-induced vibrations in weld joints may improve the structure's integrity owing to the risk of failure. In this document, a numerical study is proposed with the purpose of predicting and measuring the vortex shedding on the helical-twisted cylinder. Different design scenarios of the groove's pitch and height are carried out, so their influence can be evaluated. Thus, the following problem statement is stated:

How influences the helical-twisted geometry the vortex shedding? And how do groove's height and pitch impact the phenomena?

Chapter 2

Background

2.1 The Strouhal-Reynolds Number Relationship

When it comes to list the parameters that influence the impact level of the vortex shedding and VIV, the Reynolds number is regarded as one of the most important. This dimensionless number is defined by the ratio between the inertia and viscous forces of the crossflow.

$$Re_D = \frac{\rho UD}{\mu} \tag{2.1}$$

Where ρ, μ, D and U are the fluid density, dynamic viscosity of the fluid, diameter of the cylinder and free-stream velocity, respectively. Different regimes will take place depending on the Reynolds number value, these are visualised in Figure 2.1.

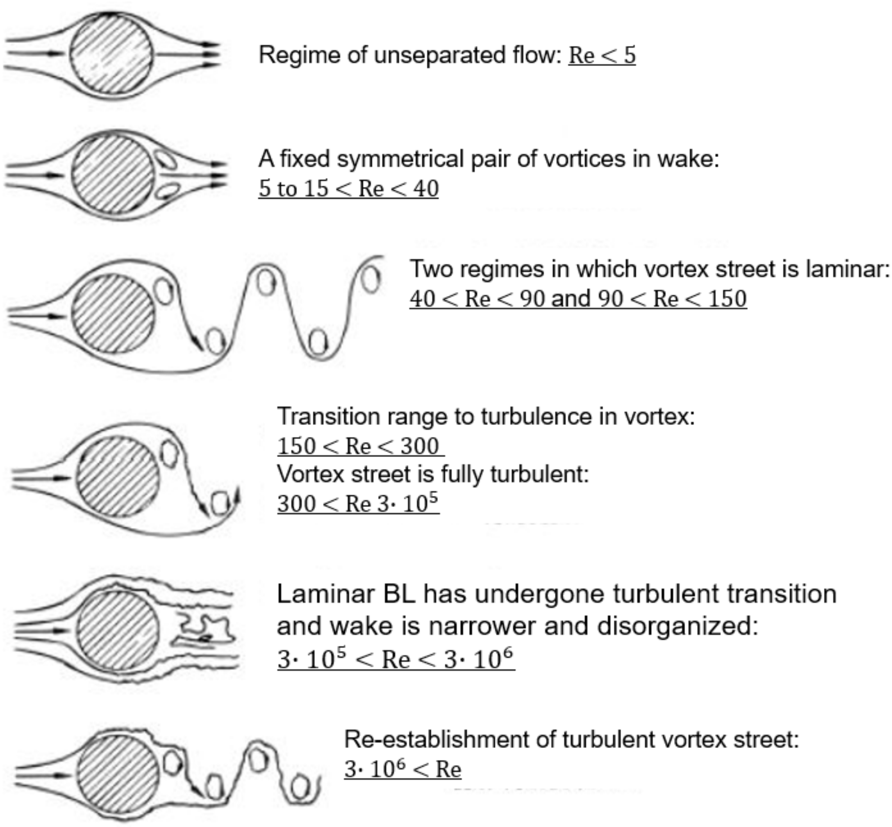

Figure 2.1: **Regimes of fluid flow across a circular cylinder [3]**

From significantly small values of Reynolds, around 5, symmetrical vortices start to appear at the near wake at both sides of the cylinder. They increase linearly as the Re and their instability increases.

When reached the value of Re = 300, the flow falls within the subcritical region. Here, the created vortices near the wall detaches from the symmetric form, thus crating a pressure gradient in the wake. Thereby creating the vortex shedding and the Kármán vortex street. The flow becomes more and more turbulent up to $3{\cdot}10^5$.

Further this limit, the transitional regime is achieved: $3{\cdot}10^5 < Re < 3.5{\cdot}10^6$. Here, three-dimensional effects disrupt in the regular vortex shedding process and the spectrum of shedding frequencies is broadened. For greater Re ($Re > 3.5{\cdot}10^6$), in the super-critical region the regular shedding is reestablished with a turbulent cylinder boundary layer.

More accurately, *Henderson et al.* declares in his work that in a flow passing a circular cylinder case, the vortex shedding emerges at $Re \approx 47$ [21]. This value is significantly small, therefore it can be concluded that it is very easy for most of the bluff bodies, like the helical-twisted pipe, to normally be subjected to vortex-induced vibrations.

Another important parameter that is worth mentioning alongside the Reynolds number is the Strouhal number (Sr). This dimensionless coefficient has an enormous importance when studying unsteady and oscillating flow phenomena, commonly seen in the cases of immersed cylinders subjected to crossflow, as discussed in this report. This can be expressed as the ratio between inertial forces owing to local acceleration and convective inertial forces. The former is referred to the the flow unsteadiness, the latter is associated to changes in velocity from point to point in the flow field [22], thus giving the following equation:

$$Sr = \frac{fD}{U} \tag{2.2}$$

Where f stands for the vortex shedding frequency.

So far, it has been described that at different Reynolds number the type of vortex shedding changes, whereby influencing in the frequency. Consequently, this leads to the conclusion that there may be a correlation between the Reynolds and Strouhal number. By following this criteria, researchers have carried out investigations in order to answer the question of how the relation can be physically expressed and represented.

It was *Strouhal* [23] who first measured that Sr number and its relation to the Reynolds number. A functional relationship was formulated in the early 1900 by *Rayleigh*, where this Strouhal number could be expressed in terms of a Taylor's expansion with the inverse of the Reynolds number [24].

$$Sr = \frac{fD}{U} = A + \frac{B}{Re} + \frac{C}{Re^2} \tag{2.3}$$

The Strouhal-Reynolds-number relationship for a flow past a circular cylinder is a well-known field of study, unlike for other geometries. Several empirical and semi-empirical formulas have been proposed to explain the Sr-Re relationship by the use of curve-fitting coefficients and physical properties related to vortex shedding. Following these attempts to formulate the St-Re relation, *Roshko* [25] plotted Sr-Re for the laminar regime, and thus found curve-fitting coefficients (A and B) from a linear-squares fit: Sr = A + B/Re. This corresponds to the first two terms of the aforementioned Rayleigh's expansion.

Roshko first suggested that the transition to turbulence is accomplished at $Re \approx 300$. In addition, it was plotted what was from then on known as the Roshko number ($Ro = Sr\,Re = fD^2/\nu$) against the Reynolds number, presenting the same fitting pattern.

On the other hand, *Williamson et al.* [19] studied the transition regime from laminar 2-D flow to turbulent and three-dimensional (Re = 230-260), being the relation linear until reached this point. Here, they took into account the variation of the shear layer thickness with $\mathrm{Re}^{-1/2}$, until at least Re = 1200 [26].

$$Sr = A + \frac{B}{\sqrt{Re}} \tag{2.4}$$

With regard to the subcritical region (300 < Re $3{\cdot}10^5$), *Fey et al.* [27] studied the Re-Sr relation with a semi-empirical approach. Here it was found that the Strouhal number reaches a constant value of 0.20 and above this range flow enters the transcritical regime Re$\approx 3{\cdot}10^6$, then increasing exponentially.

In another of his works, *Roshko* [28] begins to take the degree of bluffness of the body on the vortex-shedding frequency into account. Hence, suggesting that the body would scale better with other parameters, thus giving:

$$Sr^* = \frac{f\,D'}{U_s} \tag{2.5}$$

Being Sr^* the wake Strouhal number, U_s the velocity at separation and D' the wake width. Three different bodies (flat plat, 90° wedge and circular cylinder) measures an universal Sr^* of 0.16 ± 0.01.

Hence, there is empirical evidence of the correlation between both of the dimensionless numbers. In fact, the distribution of the relationship's data has been plotted by numerous researchers, achieving the same shape and coming to the same conclusion: Sr has a constant value of 0.20 in the range of $3{\cdot}10^2$ < Re < $3{\cdot}10^5$, thus being an accurate assumption for the circular cylinder case. This can be seen in the following Figure 2.2:

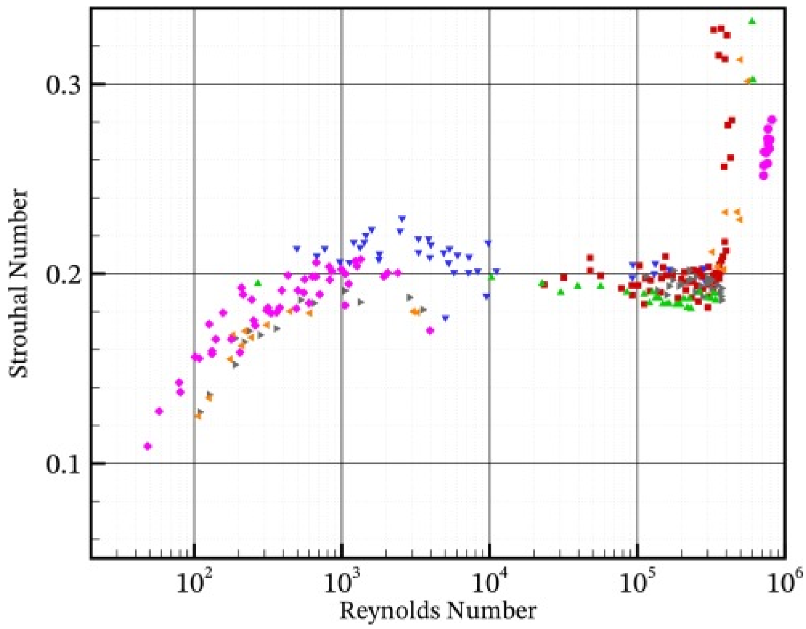

Figure 2.2: **Strouhal-Reynolds relationship, empirical data from different sources [29]**

In the Figure the 4 different regimes of vortex shedding can be seen. From low-Reynolds the Strouhal number increases with a linear behavior until reaching the sub-critical region at Re $\approx$ 300.

From here, the Strouhal number reaches a constant value of 0.2 unto the transitional regime, where it decreases slightly its value. Further this limit, in the super-critical region the Sr significantly rises for every increased unit of Re.

It is frequent among the scientific community to consider the Sr number to have constant value of 0.20 within the sub-critical regime. However, according to the spread of research results in Figure 2.2, it can be noticed that there is a wide fluctuation in the resulting Sr number, where it seems to be constant at values of 0.18.

It is significantly easy for the case of circular cylinders to fall within the range of constant Strouhal number, with relative small diameters and free-stream velocities. Therefore, it becomes a valuable parameter of design for vortex shedding modelling and the assessment of flow induced vibrations. With regard to the helical-twisted cylinder, since the oscillations are expected to decrease due to the geometry, the vortex shedding frequency may decrease as well and so its Strouhal number.

2.2 Aerodynamic Force Coefficients

As a result from the interaction between body and crossflow, axial and normal forces take place in their interface. These forces can be expressed as wall shear stress derived from the friction due to viscosity and normal stress, given by the pressure distribution, respectively [22]. At every point in the body, both stresses take place, but the summation of each one of them yield the resultant drag (F_D) and lift forces (F_L), where the former is parallel to the freestream velocity direction and the latter normal to it.

In order to calculate the forces, the estimation of the drag and lift dimensionless coefficients has become commonly used. At the same time, these estimations can be either determined by experimental studies or by numerical analysis. Both methods are carried out and detailed in this Master thesis document.

Therefore, drag coefficient (C_D) and lift coefficient (C_L) expressions in the case for a cylinder are as follows:

$$C_D = \frac{F_D}{\frac{1}{2}\rho DLU^2} \tag{2.6}$$

$$C_L = \frac{F_L}{\frac{1}{2}\rho DLU^2} \tag{2.7}$$

Where the characteristic area (A) is the frontal area, which at the same time is the diameter times the length of the pipe.

2.3 LES as the Chosen Numercial Model

Generally an immersed body in a flow can be classified among three different categories: two-dimensional, axis-symmetric and three-dimensional [22]. A circular cylinder has been frequently tested under the assumption of two-dimensional. However, the near wakes created from the induced vortex cannot be classified as so, but rather three-dimensional. Thus, this approach appeals as insufficient. So far, the lack of work in the three-dimensional numerical studies of immersed bodies was based on the weight of computational time and effort, which can be added up if the difficulty involved from complex body geometries, which are the characteristics given in the helical-twisted cylinder case.

In a fluid mechanics problem, the equations of continuity and Navier-Stokes are the ground rule on which the modelling is based. However, different methodology can be employed in order to describe the behavior of the fluid performance. When it comes to turbulence model, one alternative is decomposing the Navier-Stokes instantaneous variables into a time-averaged mean and a fluctuating component, which alongside the continuity equation, define the Reynolds Average Navier-Stokes (RANS) equations. Another option would be the LES model, which employs governing equations that obtained by filtering the time-dependent Navier-Stokes equations in either Fourier space or configuration space [30]. This filtering process consists in taking into account the larger eddies dynamics by limiting the scale of these eddies, thus taking out the smaller ones than the stated width or grid spacing. Hence, this process provides a reduction in the computational cost by ignoring expensive loads of small calculations, thus giving a much refined computational mesh. This advantage can turn into a handicap for cases in which small-scales eddies have a major importance and impact such as in near-wall flows.

RANS modelling statistical averaging leads to a steady system of equations for a two-dimensional flow with large length and time scales. Therefore, the computational costs regarding this modelling are the most affordable among the all the options. RANS approach has been used in numerical predictions of laminar and turbulent in FSI applications. However, flow predictions involving large-scale flow structures such as vortex shedding are often not reliable predicted by RANS. More advanced Techniques, such as LES are required. To resolve turbulent flow field in time, LES uses small time steps. Hence, in general explicit time-marching schemes are favored, especially predictor-corrector schemes. Due to deformations in the structure, the solution domain changes in time, resulting in moving grids that affect the filtering process of LES. [31]

However, the lack of resolved motions does not enable RANS to simulate instabilities, whereas LES is capable of simulate fluctuating three-dimensional turbulence structures. This is why, between both options the use of LES is often preferred for achieving more accurate flow simulations [32], thus making it the selected scheme for designing.

On the other hand, these are not the only ways for CFD modelling. Theoretically, all the scales present in a fluid can be numerically solved in a turbulent flow, needing the mesh to be fine enough to resolve the Kolmogorov scales. This method is known as Direct Numerical Simulation (DNS). Nonetheless, the large computational expenses that implies the model makes it only feasible for simple geometries and low Reynolds number [33], which is something very restrictive for the case presented in this project. Hence, the LES model remains as the most suitable model for the helical-twisted pipe simulations.

An substantial parameter that is important to keep an eye on with regard to LES simulations, is the dimensionless wall distance (y^+). This concept is associated with the boundary layer (BL) theory. In laminar boundary layers, this region is the layer affected by viscosity forces. However, in turbulent boundary layer this kind of differentiation cannot be applied. In this scenario, the flow gets divided into outer flow (turbulence free) and the turbulent flow characterized by randomized motion within the boundary layer. Here, in a turbulent boundary layer the effect of the friction forces due to viscosity is confined to a thinner layer adjacent to a wall, this region is called the viscous sublayer [34].

Depending on the value of the y^+, a determined resolution is achieved by an exact cell size adjacent to the wall. In order to achieve a correct resolution in the viscous sublayer, this value has to fall within this range: ($0 \leq y^+ < 5$). Nonetheless, when it comes to LES numerical models it is recommended to keep this value between 0 and 1. This is due to the filtering process of LES, the smaller eddies that do not fulfill the filter have to be compensated in the model by a significantly small y^+, which can be yielded through the following equation

$$y^+ = \frac{u^* \Delta y}{\nu} \tag{2.8}$$

Where u^* is the wall friction velocity, Δy is the distance of the adjacent element to the wall and ν is the kinematic viscosity of the fluid. At the same time:

$$u^* = \sqrt{\frac{\tau_w}{\rho}} \tag{2.9}$$

Being τ_w the wall shear stress.

$$\tau_w = \mu \left(\frac{\delta u}{\delta y} \right)_{y=0} \tag{2.10}$$

2.4 Geometry And Fluid Properties

A total of six different cylinder bodies are studied in this report: a regular circular cylinder and 5 different helical-twisted cylinder configurations. The circular cylinder is introduced as a preliminary analysis, whereby the pressure, velocity and vortex shedding frequency are obtained in order to evaluate the LES model suitability. Thus, the impact of the geometry in the vortex shedding can be contrasted and evaluated at same conditions: same dimensions and crossflow.

The cylinders have 114 mm of diameter and 8 mm of thickness, being hollowed within it. These dimensions were taken from a former standardized strength study carried out by *NordBase*, whose information was provided by Torben H. Pedersen from AcuRail. This document is available in Appendix A. With regard to the length, in the report the pipe was tested with a 6412 mm distance from side to side, where they were held with bearing supports. However, this dimension is not feasible for numerical simulation, hence, smaller lengths can be employed to fulfill the requirements and get representative values out of a LES simulation. These dimensions are discussed in the following Chapter 3.2.

In Figure 2.3, the six different cylinders are shown with their respective dimensions. Regarding the sinusoidally corrugated pipes, the pitch (p) and the height (e) of the groove are usually classified in terms of cylinder's diameter. Case d) with p/D = 1 and e/D = 0.1 was chosen for the test convergence test, due to its sufficiently large design for height and groove, which can be compared with their different degrees. From here, b) and c) are compared to this scenario with constant pitch but different height, whereas e) and f) are compared with constant height and variable length.

Table 2.1: **Cylinder cases with its dimensions**

Case	**Description**
a)	Circular
b)	p/D = 1.0, e/D = 0.05
c)	p/D = 1.0, e/D = 0.20
d)	p/D = 1.0, e/D = 0.10
e)	p/D = 0.5, e/D = 0.10
f)	p/D = 2.0, e/D = 0.10

All cylinders were designed using Inventor 2020 software and then exported to a CAD file with a STL extension. This format defines the body of the cylinder in the meshing process, explained further in Chapter 3.2.

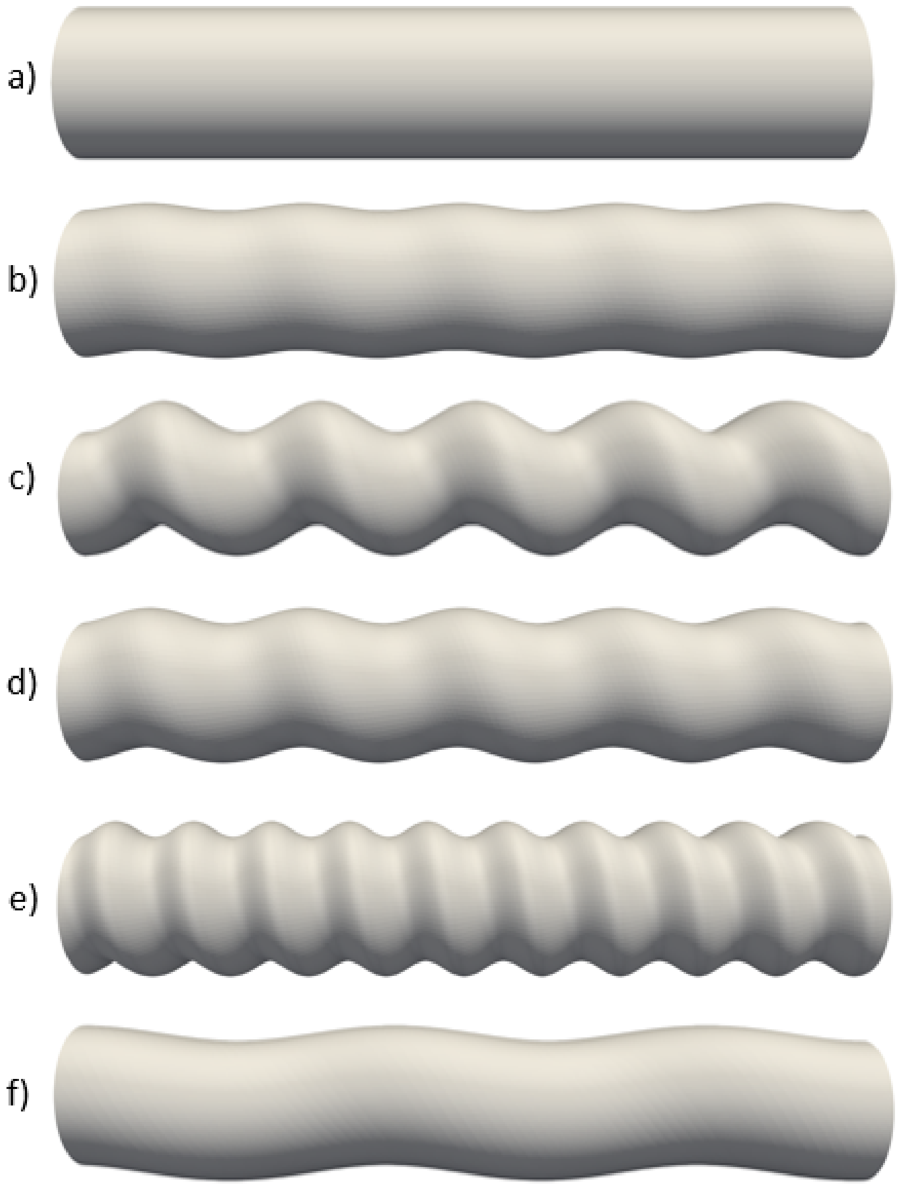

***Figure 2.3:* From top to bottom: a) Circular, b) p/D = 1 e/D = 0.05, c) p/D = 1 e/D = 0.2, d) p/D = 1 e/D = 0.1, e) p/D = 0.5 e/D = 0.1 and f) p/D = 2 e/D = 0.1**

For the project analysis, the cylinders are subjected the air crossflow. The physical properties of the air are considered to be at standardized sea level conditions of 1 bar and 20°C of pressure and temperature, yielding a density (ρ) and a dynamic viscosity (μ) of 1.205 kg m^{-3} and 1.82·10^{-5} kg m^{-1} s^{-1}.

The vortex shedding of a circular cylinder with the described dimensions appear under significantly small air velocities. For instance, a velocity of 1 m s^{-1} give a Re = 2280 and a vortex shedding frequency of 1.75, with Sr = 0.2.

The cylinders are considered to be brought under normal velocity air conditions on shore. The annual average wind speed in Denmark, more accurately in the area of Esbjerg, goes from around 5-7.5 m s^{-1} [35], thus falling within the range of subcritical region. In addition, the air velocity used in the report from *NordBase* was 5 m s^{-1}. Therefore, a value inside the subcritical range of with Re = $3.7 \cdot 10^4$ was chosen for the simulations.

Chapter 3

CFD Modelling

For the CFD computation, the open source OpenFOAM v7 is used for the design and the numerical analysis. The simulations have been running parallel with a multi-processor computer (Intel Xeon(R) CPU E5-2637 v4 @ 3.50GHz x 16) provided to the student by the Thesis supervisor Matthias Mandø. Here, a LES simulation of 15 seconds with 3.3 million cells circular cylinder, with the eight available processors can take about 24 hours and 29 min, whilst for an helical-twisted p/D = 1 e/D = 0.1 takes up to 3 days and 16 hours of simulation.

In this section, the numerical studies on the circular and five other helical-twisted cylinders are carried out. An important step in every model is the assumption accounting, which are the base of the calculations. For this purpose, the air crossflow is regarded as incompressible and isothermal flow. Thus, these assumptions defined a simple analysis, which can save a heavy load of computational time and enabling the development of the project to focus on the prediction of the flow-body interface mechanics.

The decisions made are described step by step from the domain definition and its mesh convergence testing to the calculation of the vortex-induced vibrations. An important step in every model is the assumption accounting, which are the base of the calculations.

3.1 Governing Equations

By following the stated hypothesis, the filtering operation give the following filtered continuity equation:

$$\frac{\partial}{\partial x_i}(\rho\,\bar{u}_i) = 0 \tag{3.1}$$

Where $\bar{u}_i$ is the filtered velocity component at the x direction in Cartesian coordinates. With regard to the Navier-Stokes equations, its filtered form in Cartesian coordinates is yielded as:

$$\frac{\partial}{\partial t}(\rho\,\bar{u}_i) + \frac{\partial}{\partial x_j}(\rho\,\bar{u}_i\bar{u}_j) = -\frac{\partial \bar{p}}{\partial x_i} + \mu\frac{\partial}{\partial x_j}\left(\frac{\partial \bar{u}_i}{\partial x_j} + \frac{\partial \bar{u}_j}{\partial x_i}\right) - \frac{\partial \tau_{ij}}{\partial x_j} \tag{3.2}$$

Here, t, $\bar{p}$, and τ_{ij} account for time, filtered pressure field, stress tensor due to molecular viscosity and subgride-scale (SGS) stress, respectively. At the same time, this last term is yielded as:

$$\tau_{ij} = \rho\bar{u}_i\bar{u}_j - \rho\overline{u_i u_j} \tag{3.3}$$

The nonlinear filtered advection term $\overline{u_i u_j}$ requires knowledge of the unfiltered velocity field, which are unknown and are modeled as:

$$\tau_{ij} = -2\mu_t \bar{S}_{ij} \tag{3.4}$$

This SGS stress resulted from the filtering accounts for the unresolved motions on the velocity field. Therefore requires modelling in terms of eddy-viscosity modelling parameters in the subgrid-scale turbulent viscosity (μ_t). The term $\bar{S}_{ij}$ is regarded as the rate-of-strain tensor for the resolved scale, which is:

$$\bar{S}_{ij} = \frac{1}{2}\left(\frac{\partial \bar{u}_i}{\partial x_j} + \frac{\partial \bar{u}_j}{\partial x_i}\right) \tag{3.5}$$

There are different modelling possibilities for μ_t with guaranteed satisfactory results. The oldest and most frequently used one is the *Smagorinsky* approach, in which the eddy viscosity is considered to be proportional to the subgrid characteristic length scale and the local rate-of-strain [36]. The limitations of this assumption derive in the development of different variations, from the Dynamic Smagorinsky model, which uses a grid and a test filter to the equations of motion, to the wall-adapting local-eddy (WALE) model. The latter is based on an invariant tensor and returns the correct wall asymptotic (y^3) behavior at wall-bounded flows [37], as well as being suitable for LES models in complex geometries since it does not need any explicit filtering and local information to build the eddy-viscosity [38].

The third model WALE, which is based on the square of the velocity gradient tensor, ensures a natural near wall damping behavior, retaining a correct wall-scaling. This means that it may appear too dissipating far from the wall [39]. However, it is used in many FSI cylinder vortex shedding predictions on turbulent flows. *Wornom et al.* [40] assessed the applicability of the WALE to a LES prediction on a flow past a circular cylinder, coming to the conclusion that: the vortex shedding, Strouhal number, formation length of Kármán vortices, mean recirculation, aerodynamic loads and pressure distribution were correctly reproduced in the simulations.

Another worth mentioning advantage of the WALE model is that it returns a zero turbulent viscosity for laminar shear flows [30], which, in contrast to Smagorinsky modelling, allows to represent laminar behavior in the flow. Hence, the WALE model is a preferable choice to fulfill the eddy-viscosity modelling requirements of the study. In the WALE model:

$$\mu_t = \rho\, L_S^2 \, \frac{(S_{ij}^d S_{ij}^d)^{3/2}}{(\bar{S}_{ij}\bar{S}_{ij})^{5/2} + (S_{ij}^d S_{ij}^d)^{5/4}} \tag{3.6}$$

Where L_S is the mixing length for subgrid-scales:

$$L_S = \min(\kappa d, C_w V^{1/3}) \tag{3.7}$$

Here, κ is the Kármán constant and d is the distance to the closest wall, V is the computational cell volume and C_w is the WALE model constant, a value of 0.325 is proven to give satisfactory results, as *Nicoud et al.* declared in their research [38, 30]. Moreover:

$$S_{ij}^d = \frac{1}{2}\left(\bar{g}_{ij}^2 + \bar{g}_{ji}^2\right) \tag{3.8}$$

Being $\bar{g_{ij}}$ the velocity gradient tensor (= $\partial \bar{u}_i / \partial x_j$)

3.2 Domain Definition and Mesh

The circular and helical-twisted cylinders are modeled for simulations in this section of the project.

To start with, it is important to design the domain in which the cylinders of D = 0.114 m are going to be subjected to the air crossflow, at Re = $3.7 \cdot 10^4$. While running the simulations, the cylinders are fixed. The limits of this domain need to be sufficiently far away from the cylinder in order to avoid unexpected influences near the body, it is common to scale the boundaries' dimensions proportionally to the diameter.

Regarding the height and width (W) of the domain, researchers do not agree in a one universal configuration, since these are designed depending on the preferences of the study. When it comes to a cylinder vortex shedding analysis, it is frequent to go from 20D to 30D height and between 50D and 60D of width. In Figure 3.1 the chosen dimensions of the domain can be seen, the limits at the top and at the bottom are 10 D away from the center of the cylinder, which is also the coordinates origin. The body is located 10D downstream from the inlet area of the flow, whereas the outcoming area is 30D away, see Figure 3.1. In a previous study, *Gao et al.* [8] found that the effect of the domain width is negligible if the blockage ratio D/W is less than 0.05. The designed total width is 40D, which fulfills this aspect. This configuration bears resemblance to numerous cylindrical vortex shedding studies [16, 15, 7].

The left side here has a shorter dimension since the undisturbed flow has no interest in the analysis, but rather the vortex shedding generated to the right side of the cylinder. Regarding the depth of the domain, *Prsic et al.* stated in their work that a length of 4D is sufficient to simulate the correlation length of a circular cylinder [41, 16], but 5D has been chosen as a cautious distance measure for the z axis.

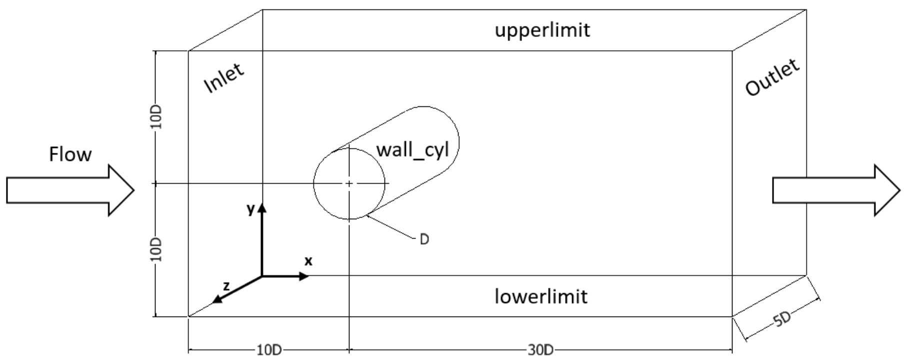

Figure 3.1: **Not-on-scale representation of domain dimensions with boundary conditions**

Meyer et al. used the same configuration for their comparison of squared and circular cylinder prediction of vortex shedding with LES, giving satisfactory results [42].

For the three-dimensional meshing, hexahedral cells are employed for the whole domain. In order to ensure the accuracy of the simulations in the region close to the surface, a subdomain around the wall of the body is defined, thus dividing the domain into different regions. First into two halves, being the left-handed side divided as specified in Figure 3.2 with three distinct layers, in order to achieve a correct grading between the meshing elements. The square shaped area in the center surrounds the cylinder, having its center at the coordinates origin, so it covers symmetrically the body spanwise.

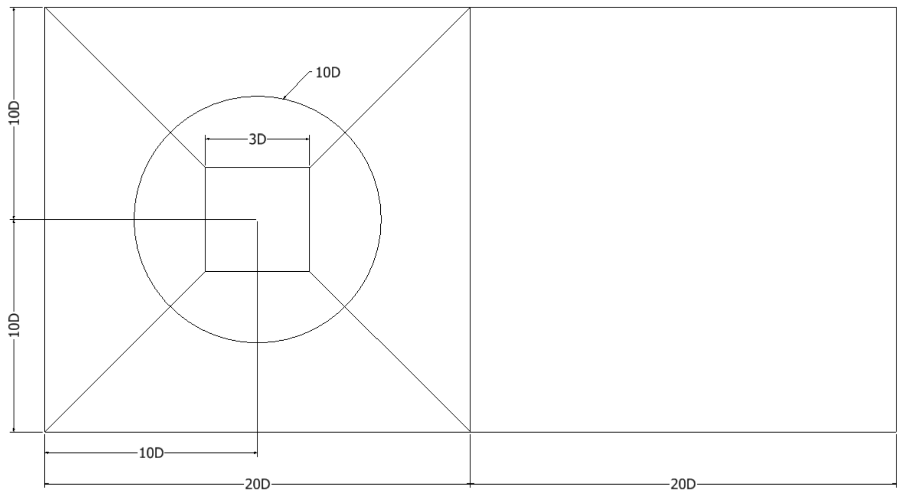

Figure 3.2: **Not-on-scale definition of the domain division**

This shape was chosen due to the chosen OpenFOAM utility for meshing called *snappyHexMesh*. This command uses CAD files with STL extension to position the body of interest inside a background mesh domain. This background is developed by a basic command from the library called *blockMesh*. Subsequently, the mesh volume from the body-domain intersection of body-domain is removed and refined in the resulting surface. The outcoming mesh with the described dimensions is shown in Figure 3.3.

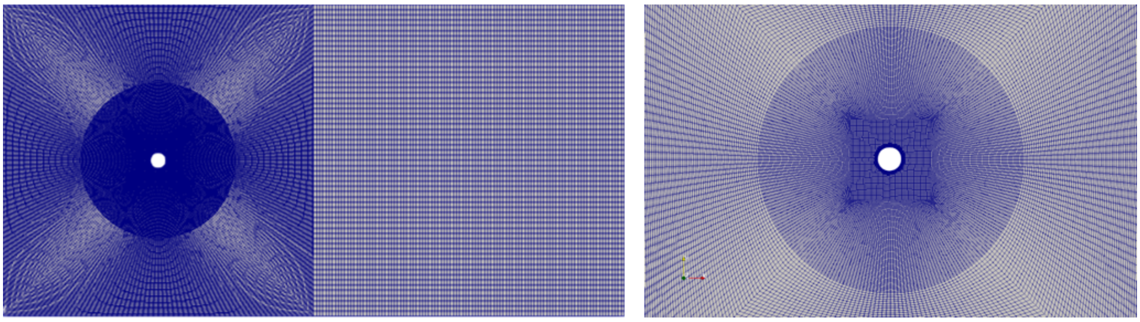

Figure 3.3: **Meshing of the domain and detail of the cylinder's subdomain in the frontal plane: at z = 5D**

In order to fit mesh cells around the circular and helical-twisted cylinders, polyhedral shaped cells are also employed. This can be seen in Figure 3.4, which was snapped from the domain within a middle plane in the z direction, at z = 2.5D. Here, a detail of the region close to the wall is given with a zoom in the right side.

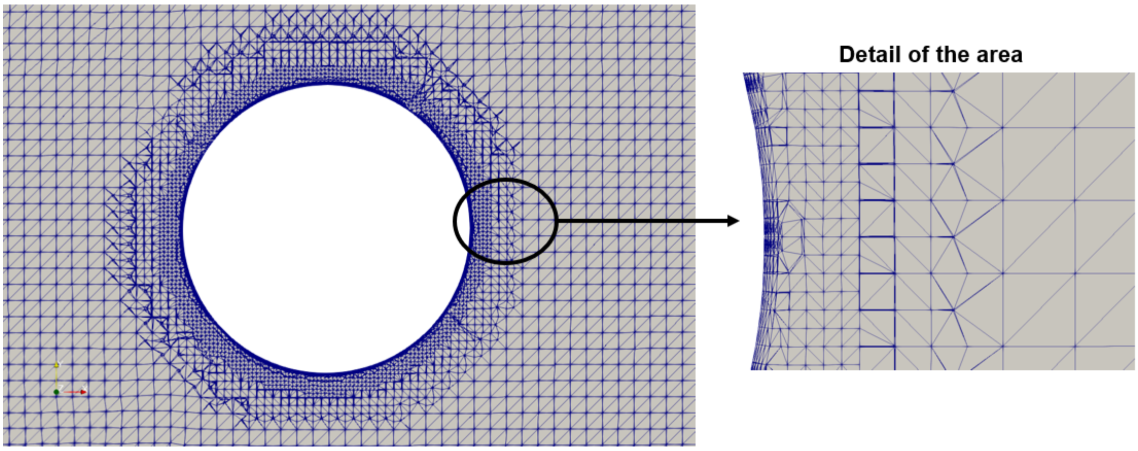

Figure 3.4: **Example from a middle plain at z = 2.5D of the different cell shapes within the domain**

To the surfaces of the domain different boundary conditions are employed, whose names can be seen back to Figure 3.1. At the inlet surface to the left of the domain, a constant horizontal velocity boundary condition is specified, whilst the outlet boundary has a zero gradient pressure condition. Apart from this, symmetry boundary layer conditions are used for the top, bottom, front and back limits. Regarding the cylinder, a no-slip condition is used, giving a zero flow velocity at the surface. A summary of this conditions can be seen in Table 3.1.

Table 3.1: **Boundary conditions summary**

Nº	Name	Type	Description
1	inlet	Constant velocity	Horizontal flow with $u_y = 0$ and $u_z = 0$
2	outlet	Constant pressure	Zero gradient pressure is imposed
3	wall_cyl	Wall	No-slip condition
4	upperlimit	Symmetry	u_x = U, $u_y = u_z = 0$
5	lowerlimit	Symmetry	u_x = U, $u_y = u_z = 0$
6	frontAndBack	Symmetry	Default surfaces limiting the control volume

With regard to the symmetry condition at the front and back planes, this was proven by *Ishibara et al.* [16] to provide an effective central symmetric and periodic pattern for aerodynamic forces prediction for long cylinders. They also state that there are two key factors that significantly influence the accuracy of simulation: One is the length of cylinder and boundary condition at the end of cylinder. Other studies support the suitability of the chosen boundary condition [43]. With regard to the ones selected for inlet and outlet patches, these are frequently used in this kind of numerical assessments.

An important characteristic of LES is that it often requires a significantly small time step, in order to achieve a correct convergence. Therefore, this parameter was subjected to study as a way to find the largest time step compatible, while keeping the numerical scheme stability. Different time step's influences were monitored for the case of circular cylinder and the different helical-twisted cylinders, thus choosing the one that minimizes the time discretization error, solution error and time of computation. The largest time step (Δt) used in the simulations was 0.001 seconds, which gave satisfactory results for the circular cylinder case. This time step gives a total of a 1000 measures/samples per second (1 kHz), this is known as sampling frequency.

Nevertheless, it was imperative to keep an eye on a fair y^+ value near the cylinder wall. For the five helical-twisted scenarios, the time step of 0.001 was insufficient, thus leading to divergence in early stages of the simulation. This is why the time step had to be reconsidered for a smaller value, after a trial-error iteration a Δt = 0.00025 seconds was found to work with satisfactory results.

One of the first steps from the numerical analysis is the definition of the total amount of time to run. For this purpose, early simulations were run for circular and p/D = 1 and e/D = 0.1 helical-twisted with a sufficiently large time period of 30 seconds. Here, the vortex shedding behavior was assessed by the aerodynamic force coefficients outcome of coarser meshes, see Figure B.1, B.5; coming to the conclusion that the pattern followed by lift and drag can be monitored successfully with smaller periods of time. Therefore, it is acceptable for the rest of the simulations to run 15 seconds in total, half of the first two trials.

The residuals are not a good indicator for the convergence for LES simulations because of the unsteadiness of the flow. Instead, certain parameters which characterizes the flow scenario like drag coefficient or total kinetic energy are commonly used for this matter.

The mesh convergence is tested by calculating the dimensionless aerodynamic coefficients of drag and lift force, plus the Strouhal number at different meshing quality. If the lift and drag follow a pattern around a constant value, the model is concluded to converge. The calculation of the latter number enables to check whether the simulations fall within the region in which the Strouhal number is constant for vortex shedding in a circular cylinder or not. Thereby, evaluating the accuracy of the simulation model. The Sr is calculated through an analysis of the lift force oscillations of the body, which matches with the vortex shedding frequency. The method used to achieve such assessment is the Fast Fourier Transform (FFT) method. Thanks to this method, the power spectrum density (PSD) of the different frequencies from the signal can be detected, being the most dominant (the most powerful), the resulting vortex shedding frequency. Then, the Strouhal number can be yielded from Equation 2.5. The FFT is carried out with MatLab software tool, whose code may be checked in Appendix C. An example of this would be the resulting graph in Figure D.2, from a simulation of 1.6 million cells. Here, it can be noticeable the predominant frequency of the signal, giving a Strouhal number of 0.19.

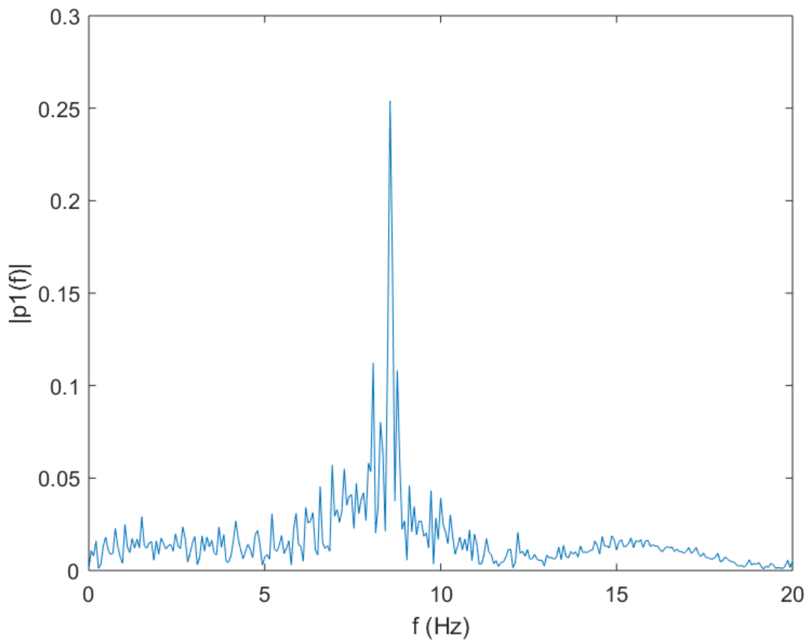

Figure 3.5: **Single-Sided Amplitude Spectrum. Signal's PSD generated by the lift force coefficient with a Mesh of 1.6 million cells for circular cylinder at Re = $3.7{\cdot}10^4$**

Generally, if the simulations were to be run with a RANS turbulence model, the PSD plot would give a horizontal line at zero, with one large peak, thus indicating the dominant frequency in the vortex shedding. However, due to the resemblance of the simulated lift coefficient to a white noise signal, there are other frequencies with an influence in the pattern of the signal. Even though, there are more frequencies to consider, there is one with the most power density, therefore, the predominant: Sr = 0.19. The appearance of more frequencies in the PSD plot may be related to the transient aspect of the LES model.

With regard to the drag and lift force coefficients, different methodology are used for extracting their resulting values out of the measurements. It can be noticed in Figure D.1 that after an early divergence in the simulation, the drag coefficient may show a convergence pattern around a final value. Therefore, the mean value of the simulation is employed (Equation 3.9), neglecting the first unstable values, which can be seen in the Figure goes up to over 0.4 seconds. This are the first 400 samples, with a sampling frequency of 1 kHz. On the other hand, the lift coefficient looks like it follows a noisy pattern in its signal, oscillating around a value of 0. This is why the root mean square is used to predict the final lift coefficient (Equation 3.10).

$$C_D = \frac{\sum C_{D_i}}{N} \tag{3.9}$$

$$C_L = \sqrt{\frac{\sum C_{L_i}^2}{N}} \tag{3.10}$$

Where N is the number of samples and C_{D_i} and C_{L_i} are the measured drag and lift at that moment.

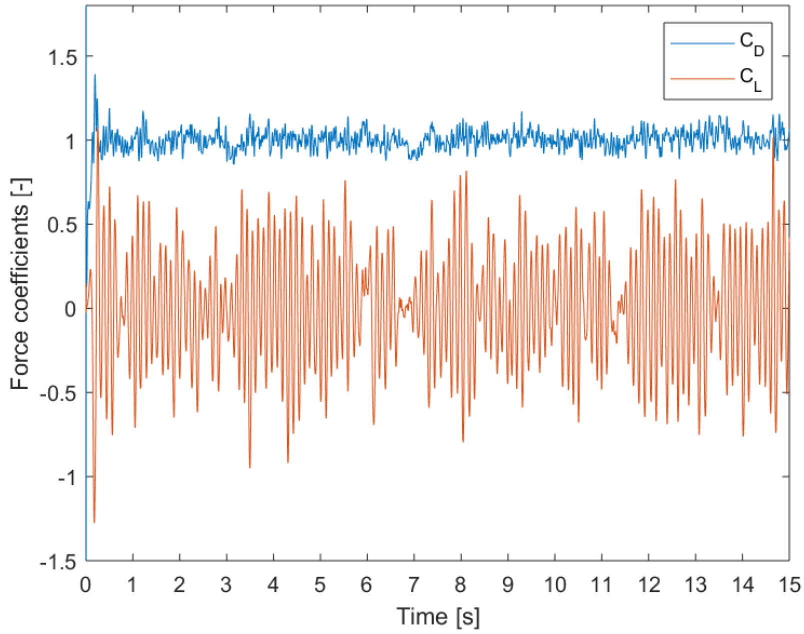

Figure 3.6: **Sampling of drag and lift force coefficients in the circular cylinder at Re = 3.7·10^4, with a 1.6 million cells**

For carrying out the test convergence two cases out of the six scenarios were chosen: circular and helical-twisted p/D = 1 and e/D = 0.1. The remaining corrugated pipe will be working under the test conclusion conditions. Here, the same reference area is employed for the simulation, thus being the diameter / characteristic length 114 mm and the longitude 5D. Besides, the same crossflow of 5 m s^{-1} is considered. Regarding the mean drag coefficient, root mean square of lift coefficient and Strouhal number, these are predicted with different mesh resolutions and represented in Table 3.2. This resolution goes under assessment by increasing gradually the number of cells in which the domain is divided, going from a much coarse meshing of around 0.8 million cells, that corresponds to the Mesh 1, to a more refined four times bigger Mesh 3, being the number of elements doubled in each stage.

In the following Table 3.2 the three scenarios for the two cylinders are represented with the resulting measured aerodynamic force coefficients and Sr.

Table 3.2: **Measured coefficients and Strouhal number at different mesh resolutions with 5 m s^{-1} crossflow**

Scenario	**Nº Cells**	C_D **[-]**	C_L **[-]**	Sr **[-]**
Mesh 1 circular	818,466	0.63±0.012	0.10±0.001	0.20
Mesh 2 circular	1,618,006	1.01±0.002	0.34±0.003	0.19
Mesh 3 circular	3,315,813	1.12±0.002	0.56±0.005	0.19
Mesh 1 p/D = 1, e/D = 0.1	818,466	1.12±0.001	0.60±0.003	0.20
Mesh 2 p/D = 1, e/D = 0.1	1,618,006	1.06±0.002	0.35±0.001	0.22
Mesh 3 p/D = 1, e/D = 0.1	3,315,813	0.84±0.02	0.18±0.001	0.23

Since the y^+ value has to be kept equal or under the value of 1 for a correct resolution of the viscous sublayer of the boundary layer, an estimation of the required wall adjacent element distance is employed by an iteration process. A representation of the y^+ convergence is represented in Figure 3.7, which was measured at the wall in the whole cylinder taking the average of the resulting maximums and minimums values.

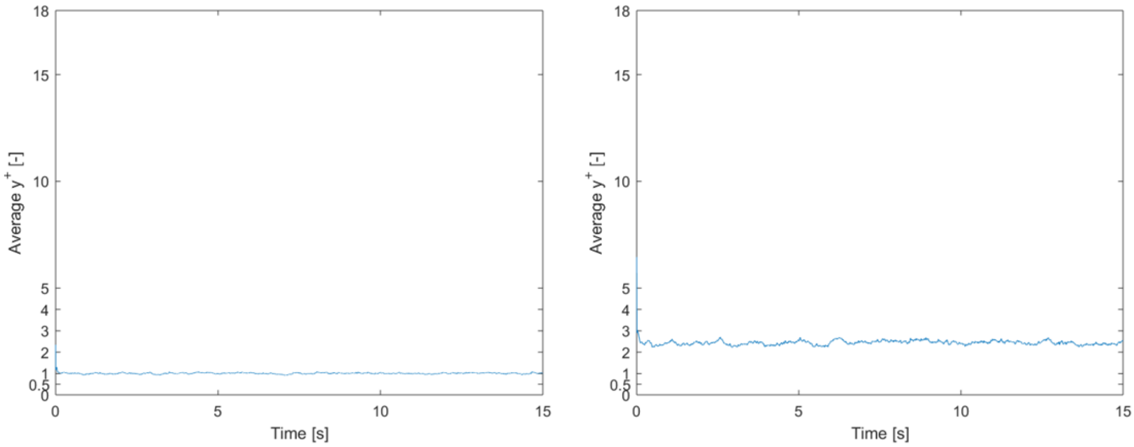

Figure 3.7: **Convergence of average y^+ vale in Mesh 2 of the circular cylinder (left side) and p/D = 1 e/D = 0.1 (right side)**

If the quality of the mesh increases, the refinement over the cylinder gets more and more complex. Unless the time step is reconsidered for a smaller, the case would not be able to converge, reaching prohibitive simulation time periods. Therefore, for different cases of helical-twisted cylinder the average y^+ was kept within the interval: $0 < y^+ < 5$. Thus, the range is wider giving more flexibility, but always keeping elements of analysis inside the viscous sublayer.

It can be noticed that for the circular cylinder, the Strouhal number achieves the expected value of 0.20 for a Re = $3{\cdot}10^4$, which corresponds to the subcritical region in a Sr-Re relationship. This happens with the three different mesh resolutions. Hence, the model is concluded to capture the vortex shedding phenomena successfully. Nonetheless, the convergence in the outcome of the yielded aerodynamic coefficients changes as the refining in the mesh grows, hence higher resolutions are preferred when simulating, which correspond to mesh 3. In addition, it can be noticed that the drag and lift force coefficients from meshes 2 and 3 differ from each other about 9.8% and 39.3% for the circular cylinder case, and 5.36% and 41.6% for helical-twisted p/D = 1, e/D =0.1 cylinder. Therefore, it can be concluded that the mesh 3 can achieve more accurate results, specially for the case of lift coefficient. However, the simulation time for 3.3 millions cells and above happens to be prohibitive for the given project time. This is why, for the sake of the project, due to the heavy loads of computational time, the mesh 2 is the chosen alternative.

Mesh 1 scenario is discarded, since for the case of helical-twisted cylinder this is unable to correctly predict the vortex shedding frequency, which was calculated to be comparable to the circular cylinder case.

The resulting sampling for the mesh 2 in a circular cylinder were already presented in Figures D.1 and D.2. With regard to the helical-twisted cylinder p/D = 1 and e/D = 0.1, it can be noticed that the vortex shedding is greater than expected at first, going up to 9.73 Hz.

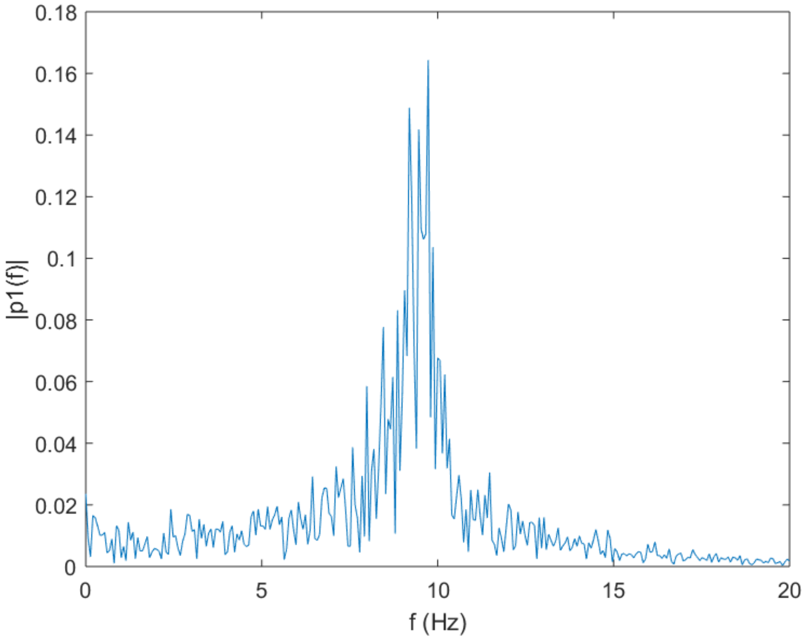

Figure 3.8: **Single-Sided Amplitude Spectrum. Signal's PSD generated by the lift force coefficient with a Mesh of 1.6 million cells for the helical-twisted cylinder p/D = 1 and e/D = 0.1**

When it comes to the sampling of the aerodynamic force coefficients, no significant difference can be detected in their followed pattern or amplitude. Nevertheless, the stability of the helical-twisted results apparently gives smoother results at earlier times of the simulation and at the end.

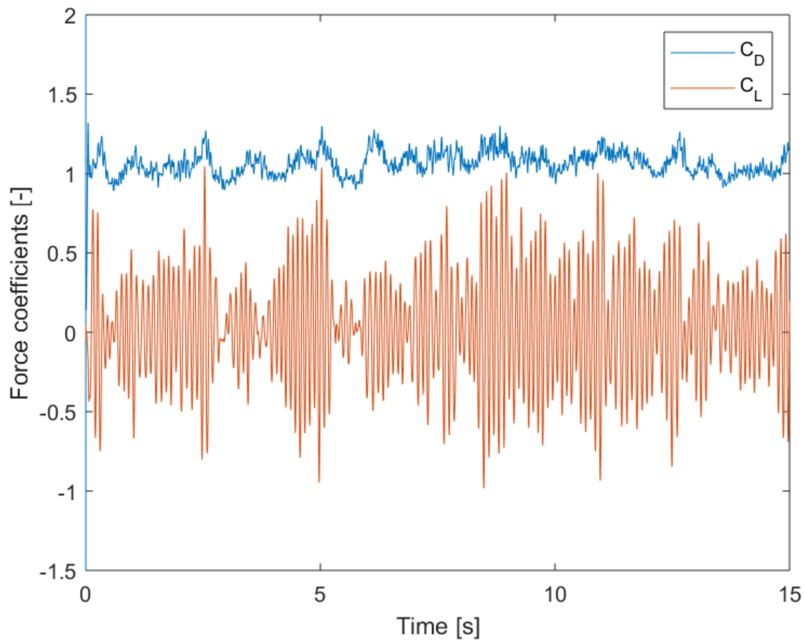

Figure 3.9: **Sampling of drag and lift force coefficients in the helical-twisted cylinder p/D = 1 e/D = 0.1, with a 1.6 million cells**

More graphs from the mesh test convergence are available in Appendix B.

The mesh properties for each case are assessed by the *checkMesh* command from OpenFOAM. For each one of them, the meshes were concluded to successfully fulfill the OpenFOAM requirements for a correct mesh, this includes the verification of: non-orthogonality, skewness, maximum aspect ratio, etc. In conclusion, the selected mesh for the circular cylinder is shown in Figure 3.10

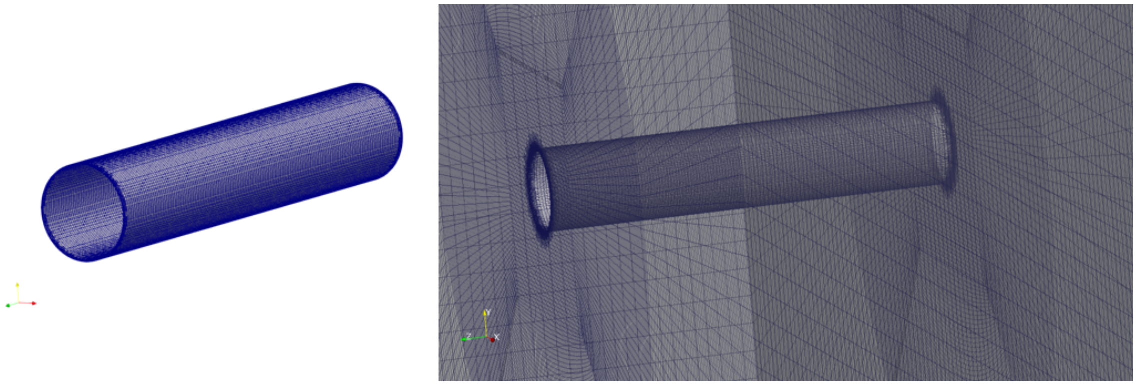

Figure 3.10: **Final mesh for the circular cylinder**

In the following Figure 3.11, the final mesh for the sinusoidally corrugated cylinder with p/D = 1 and e/D = 0.1 is presented.

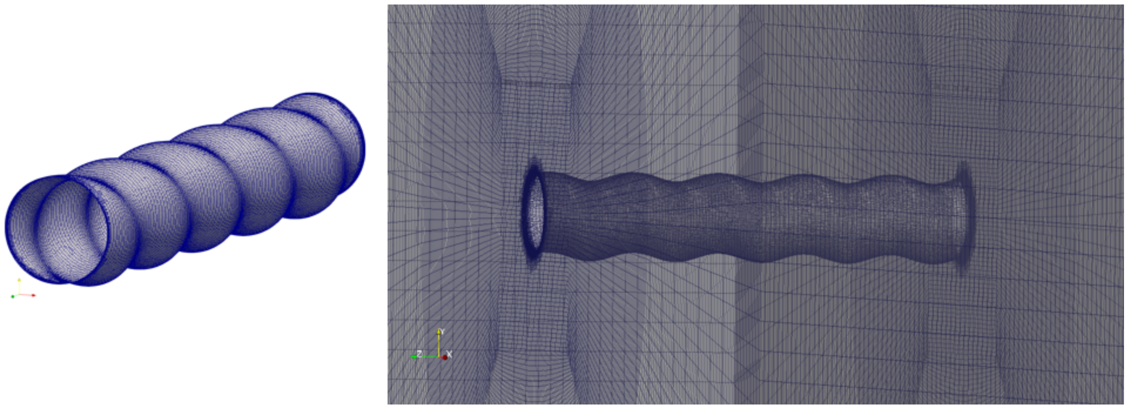

Figure 3.11: **Final mesh for the helical-twisted cylinder with p/D = 1 and e/D = 0.1**

3.3 Convergence And Discretization Method

Once the domain and the mesh for the simulations are defined, the convergence analysis and the discretization method follow.

Supporting, the aerodynamical forces test convergence described before, the average the average Courant number (Co) was monitored and kept with lower values than 1, since bigger than this threshold the simulation is expected to diverge. Therefore, this Courant number was recorded to reinforce the simulation stability as an indicator. In OpenFOAM this value is recommended to fall within the range of 0.1 and 0.5 for a correct convergence [44]. For example, for the scenarios of circular and p/D = 1 e/D = 0.1 helical-twisted cylinders, the mean Courant number reported was 0.35 and 0.09 respectively.

OpenFOAM does not provide the user with an universal solver. Instead, it has a wide variety of optional solvers for calculating the flow field variables depending on the assumptions made for the model. For this application, the PIMPLE algorithm has been chosen due to its compatibility with incompressible, transient, turbulent and Newtonian flows characteristics, thus coupling pressure and velocity. The PIMPLE name is given due to the fact that is a merged solver of PISO and SIMPLE algorithms. Furthermore, it is known that the time step in LES simulations has to be sufficiently smaller than the time scale from the filtered eddies. PIMPLE algorithm allows to use a bigger time step than another applicable solver like PISO, thanks to the inner loops than enhances the convergence and the usage of relaxation factors.

The filtered Navier-Stokes equations have been discretized using finite volume method of Gaussian integration on a fixed Cartesian space with with non-uniform meshing, which requires the interpolation of values from cell centres to face centres. The interpolation scheme is then given by the linear entry. The selected temporal discretization is the "backward" scheme of OpenFOAM for being applicable to transient and second order implicit simulations. The remaining eligible schemes were left as default.

Table 3.3: **Summary of LES simulation settings for OpenFOAM**

Setting	Specification
Type of simulation	3D
Solver	PIMPLE
Temporal scheme	Transient 2^{nd} order implicit
Gradient scheme	Gauss linear
Divergence scheme	Gauss limited linear
Surface normal gradient scheme	Corrected
Interpolation scheme	Linear
Laplacian scheme	Gauss linear corrected
SGS model	WALE
	$C_s = 1.048$, $C_k = 0.094$, $C_w = 0.325$

Chapter 4

Results

In this chapter, the simulation results from the six fixed cylinders are shown and discussed. Here, the recorded contours of instantaneous velocity (Figure 4.1) and filtered pressure (Figure 4.2), known from now on as *p*, are presented. Besides a comparison of the sampled aerodynamic lift coefficients. This combination gives as a result an insight of the flow pattern and the vortex shedding frequency. This is done for several helical-twisted cylinder alternatives, with various groove configurations groove. The flow pattern presented in both contours for circular and helical-twisted are visualized in a plane located in the z-direction, more accurately at z = 2.5D, in the middle of the domain.

For the circular cylinder the appearance of the repeating pattern of swirling vortices is noticed, defining the region of the Kármán street. Here, two single vortices are shed per cycle, where one cycle is an up and down fluctuation. Such sequence continues downstream until it dissipates. *Williamson and Roshko* [45] first introduced certain terms to refer to specific wake flow patters caused by the vortex shedding and vortex-induced vibrations. The main used terminations are 2S and 2P, which stand for 2 single vortices formed per cycle and 2 pairs of vortices per cycle. The former is associated to the early stages of the vortex shedding formation, the latter to more developed stages of the phenomena.

Even though there are more accurate variables in the detection of vortices, such as vorticity, these can be detected from the velocity magnitude contour. Here, low-velocity regions are surrounded by other adjacent regions with greater values. The vortex corresponds to the area in which the air flow is slowed down in a swirl shape. The limit of the vorteces and the high-velocity regions have the same direction. Therefore, the shedding of pair of vortices (2P) can be seen in Figure 4.1.

When suppression mechanisms are employed, this vortex shedding patterns are destroyed, thus forming a larger single group of vortices. The dimensions of the group may mitigate the pressure gradient near the wake and the vortex shedding phenomena. This group tend to merge into a single large vortex further away in the wake.

It is found that the range of velocity magnitudes varies depending on the configuration of the cylinder. For instance, it seems like in the p/D = 2 e/D = 0.1 scenario, the maximum velocity reached value goes up to 9.5 m s^{-1}, and it gets even larger for the p/D = 0.5 e/D = 0.1 up to 9.5 m s^{-1}.

For the scenario of helical-twisted cylinder with p/D = 1 e/D = 0.2, the boundary layer that delimits the near wake gets more straightened than the rest of the scenarios. This gives a wider near wake, where the vortices are shed further away from the wall of the cylinder.

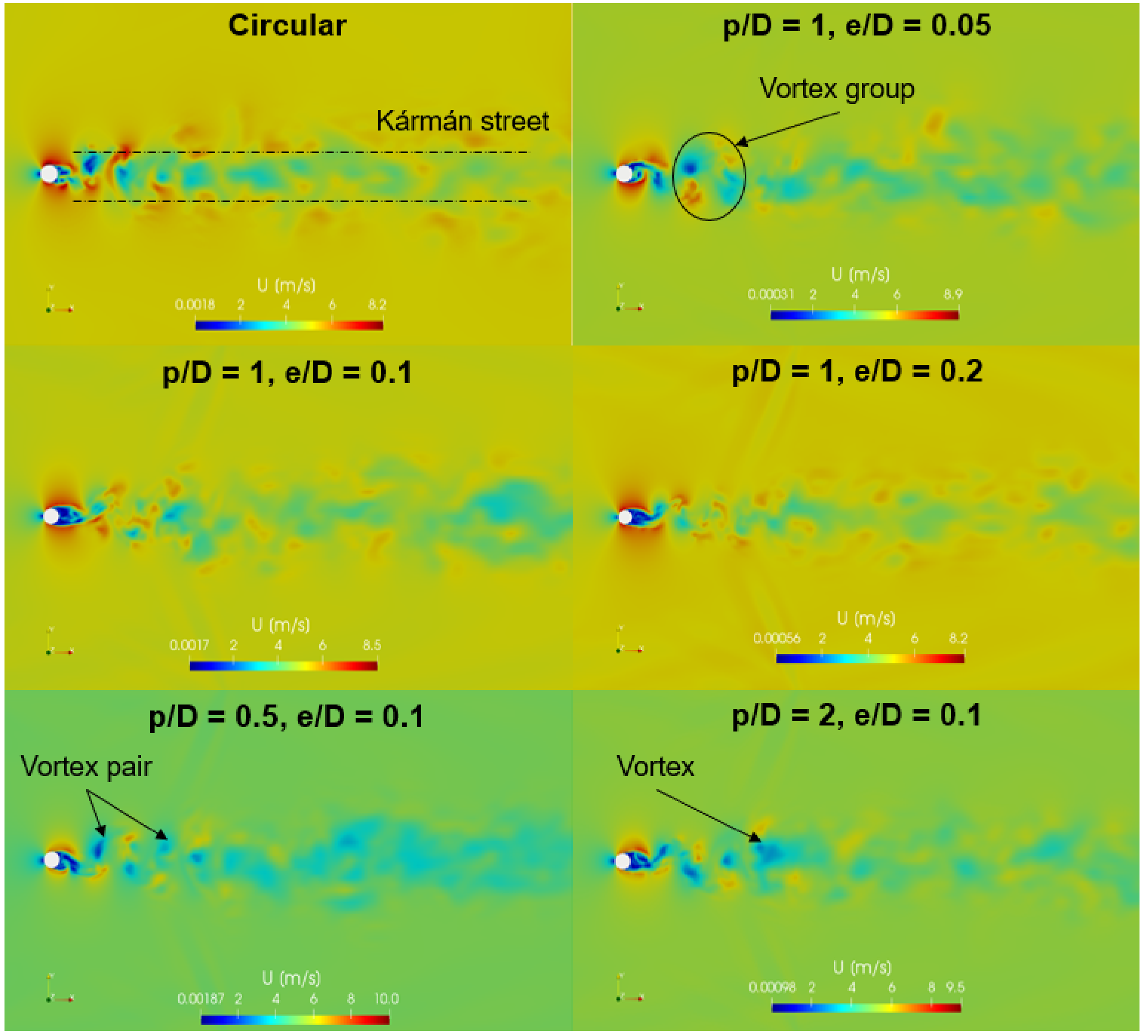

Figure 4.1: **Velocity (U) contours of the different cylinder geometries at z = 2.5D with Re = $3.7 \cdot 10^4$**

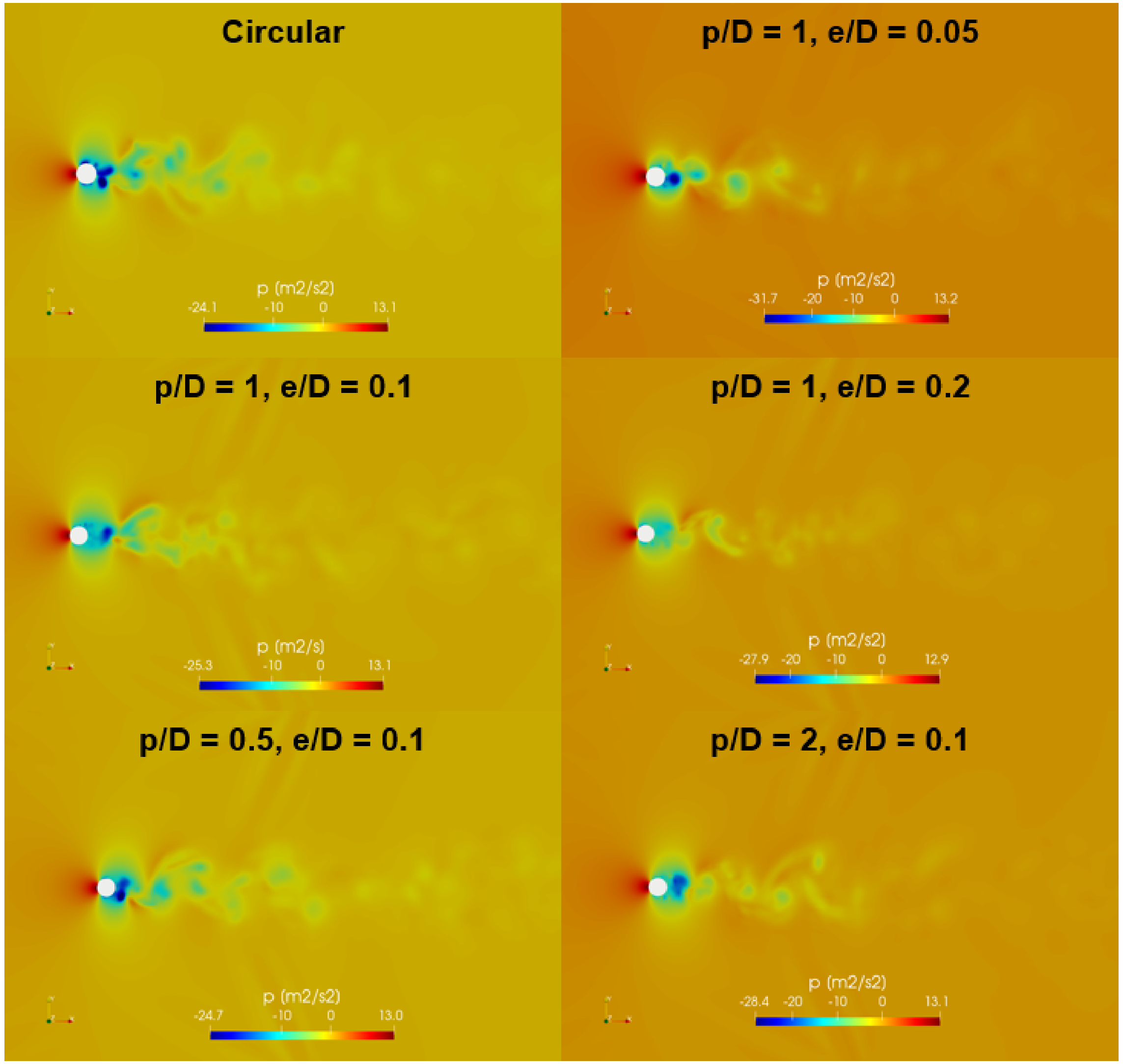

Figure 4.2: **Filtered pressure ($\bar{p}$) contours of the different cylinder geometries z = 2.5D with Re = $3.7 \cdot 10^4$**

With regard to the contours of filtered pressure, Figure 4.2 is presented. There are negative pressure magnitudes represented. This is given by the accounted approximation of incompressible flow in the Navier-Stokes equation, where the value of filtered pressure has no physical meaning, but rather its gradient. Thus, it is the driving force of the flow. If constant zero condition is stated at the outlet, regions with lower pressure tend to reach negative values.

During the vortex shedding, the formation of low-pressure regions at alternate side of the cylinder is noticed. Every time that a vortex detaches from the near wake due to instabilities in the flow, it creates an area with a great pressure gradient, which pulls the wake towards it. Such phenomena displaces the low-pressure region, thus alternating its position in the wake up and down.

Table 4.1: **Measured vortex shedding frequency and Strouhal number at different cylinder configurations with Re = $3.7{\cdot}10^4$**

Case	Description	f [Hz]	Sr [-]
a)	Circular	8.56	0.19
b)	p/D = 1.0, e/D = 0.05	7.19	0.16
c)	p/D = 1.0, e/D = 0.20	11.07	0.25
d)	p/D = 1.0, e/D = 0.10	9.73	0.22
e)	p/D = 0.5, e/D = 0.10	10.13	0.23
f)	p/D = 2.0, e/D = 0.10	10.07	0.23

The used power spectral density graphs to calculate Sr for each alternative can be consulted in Appendix D, alongside the lift and drag coefficient measurements.

From Table 4.1, it is found that the p/D = 1 e/D = 0.05 helical-twisted configuration appears to reduce the vortex shedding frequency by 16%, comparing to the circular case.

This helical-twisted cylinder of p/D = 1 e/D = 0.05 is seen as a possible configuration to vortex shedding suppression. In order to assess the mechanisms used by the body to solve this issue, a three-dimensional analysis is carried out. This assessment involves the comparison of the created vortex shedding at different plains in the z-direction of the domain: z = 1.25D, z = 2.5D and z = 3.75D.

This comparison can be seen in Figure 4.3. Here, it is observed that the range of velocities changes its values of minimum and maximum in the spanwise direction. Such changes in the velocity magnitude leads to an acceleration in the vortex shedding. This can be detected in the shift of the flow pattern present in the three different planes of the circular cylinder. With regard to the helical-twisted cylinder, the velocity range remains constant, therefore, the flow pattern variations can be considered negligible. Consequently, this information suggest that the helical twisted cylinder may improve the vortex shedding frequency reduction by influencing in the three dimensional disturbance in the spanwise direction.

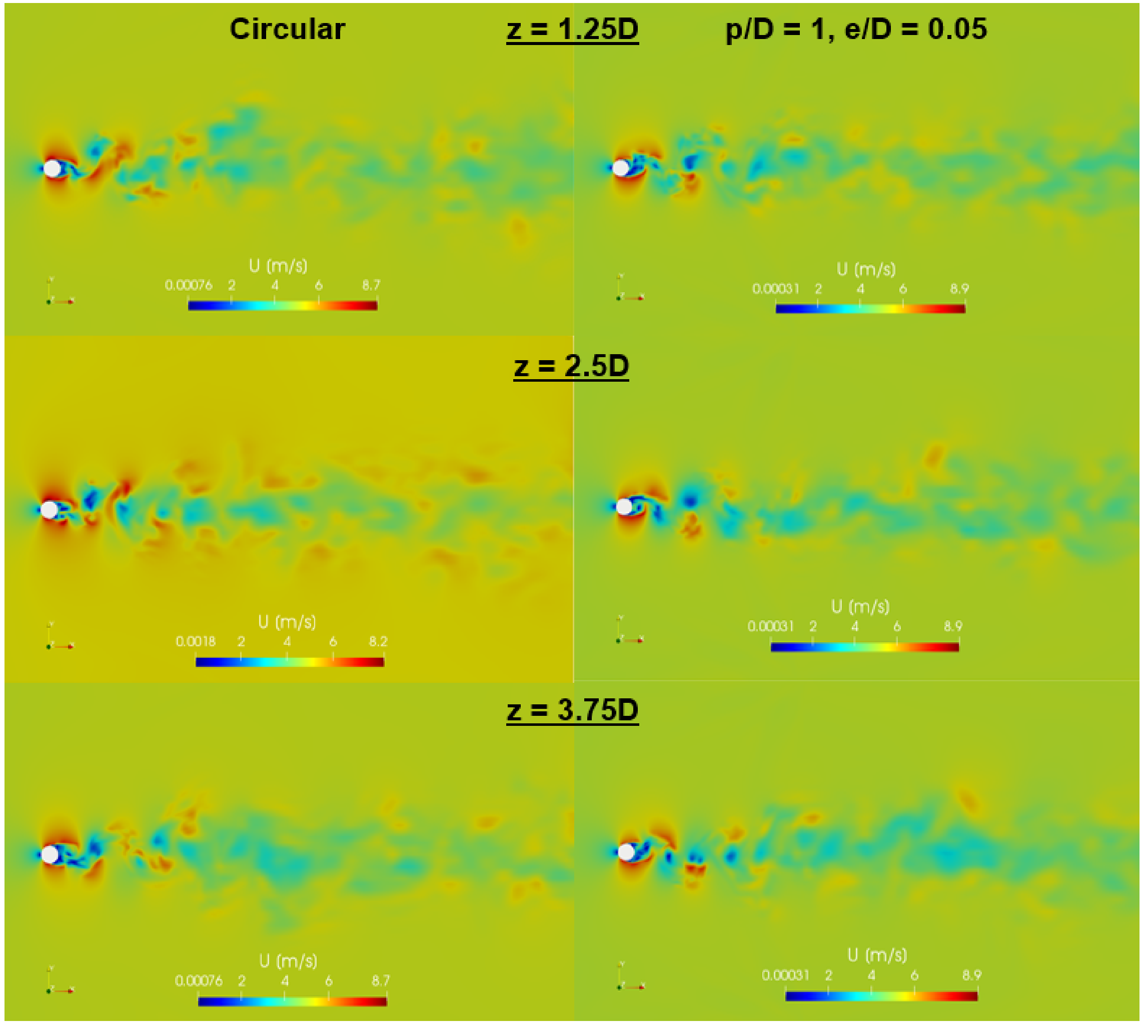

Figure 4.3: **Comparison of the vortex shedding patterns at different planes of the domain: z = 1.25, z = 2.5 and z = 3.75**

Furthermore, the shape of the surface seem to help the flow to cross without relevant disturbances without relevant accelerations, thus reducing the disturbances in the near wake and eventually in the lift force fluctuation.

It can be noticed that among the different alternatives of helical-twisted cylinder, the smaller the variation given by the twisting pattern to the surface, the better its properties to counteract vortex shedding phenomena. Therefore, it is preferable to have slight values for depth and pitch groove parameters, like the employed case in the document of: p/D = 1 e/D = 0.05.

In order to get a better understanding of the suppression mechanism, a comparison of the lift coefficient's amplitude is done and represented in the following Figure 4.4

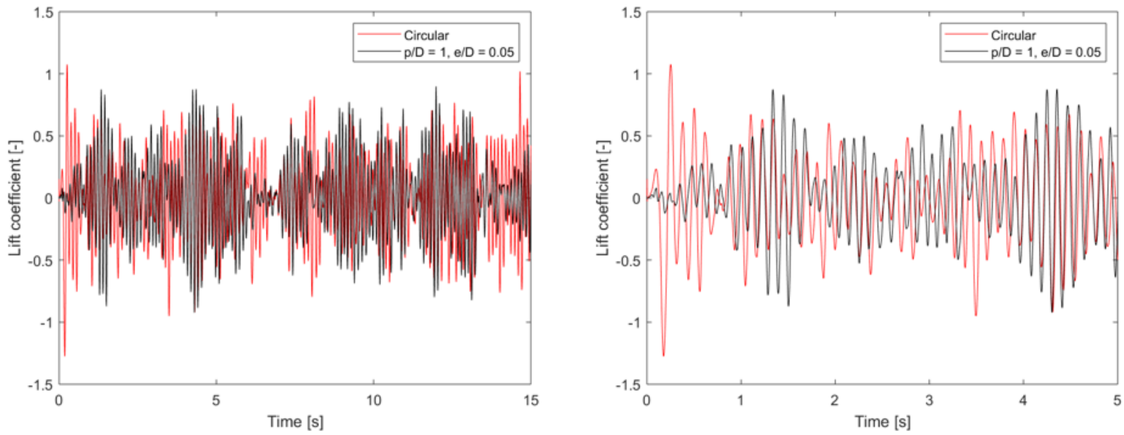

Figure 4.4: **Comparison of recorded lift coefficient from circular and p/D = 1 e/D = 0.05 cylinders. With at Re = 3.7·10^4. To the right there is a detail of the simulation's first 5 seconds**

There are periods in which the amplitude is significantly smaller than the circular cylinder. However, on average the both lift force are alike.

When the crossflow encounters the cylinder, the high-velocity profile at the upper and lower side of the body are smaller and less aggressive for the cases of: p/D = 1 e/D = 0.2, p/D = 2 e/D = 0.1 and p/D = 0.5 e/D = 0.1; when compared to the rest of the cylinders. This "smoother" profile suggests that the amplitude of the lift force generated due to pressure gradient in the near wake may be reduced. As well as, the Kármán street can be noticed to be narrower. In the following Figure 4.5, the lift force sampling of the mentioned helical-twisted cylinder are compared to the circular cylinder.

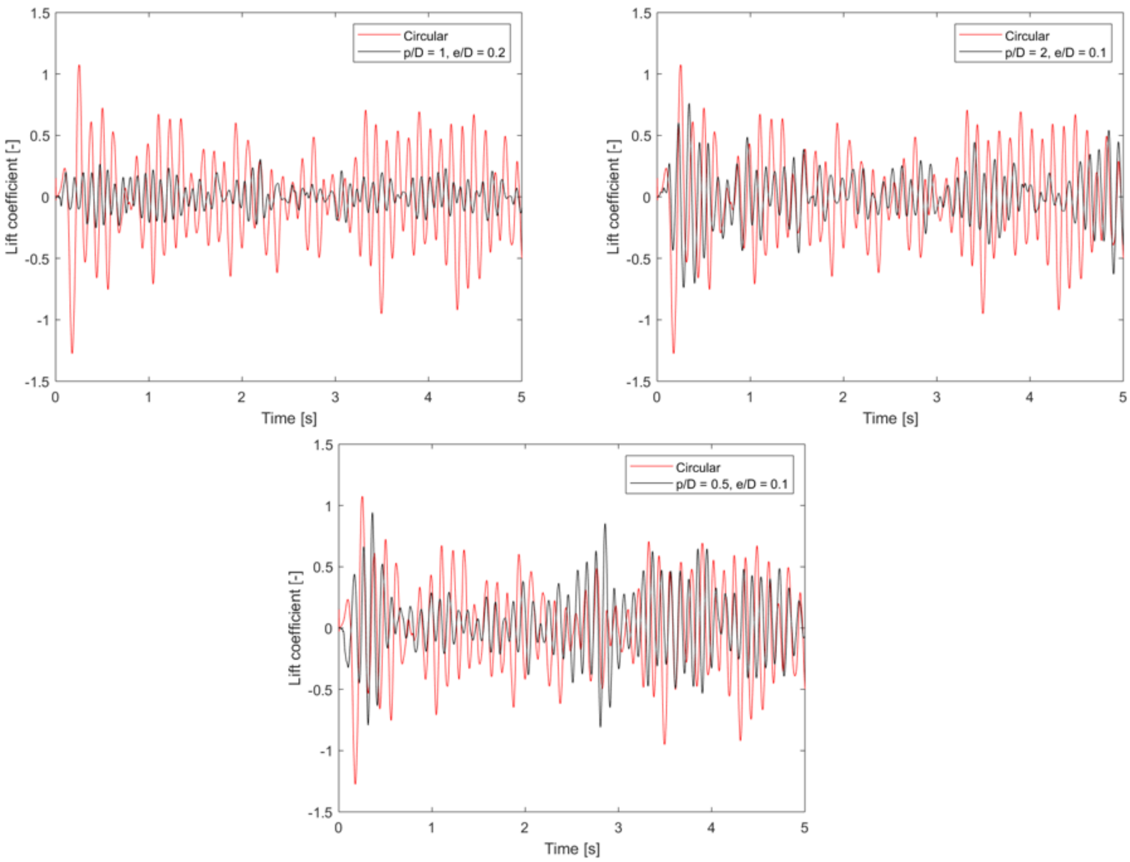

Figure 4.5: **Comparison of recorded lift coefficient from circular with: p/D = 1 e/D = 0.2 (top-left), p/D = 2 e/D = 0.1 (top-tight) and p/D = 0.5 e/D = 0.1 (bottom) cylinders; Re = 3.7·10^4**

It appears that the amplitude of the lift force fluctuations are reduced for these scenarios Therefore, this force acting on the body on the body is less strong than for the cases.

In Table 4.2, the root mean square of C_L of the scenarios are summarized. Here, the ratio of the lift coefficient is calculated with regard to the value of the circular cylinder. By following this criteria, it can be noticed that this four configurations reduce the amplitude of the signal effectively. The positives values for the other scenarios indicate an increment in the lift force amplitude.

Table 4.2: **Reduction of lift coefficient fluctuation amplitude in different cylinder configurations with Re = 3.7·10^4**

Case	Description	Mean C_L [-]	Reduction [%]
a)	Circular	0.34±0.003	-
b)	p/D = 1.0, e/D = 0.05	0.31±0.014	-8.53
c)	p/D = 1.0, e/D = 0.20	0.09±0.001	-73.5
d)	p/D = 1.0, e/D = 0.10	0.35±0.010	+2.94
e)	p/D = 0., e/D = 0.10	0.26±0.001	-23.5
f)	p/D = 2.0, e/D = 0.10	0.18±0.001	-47.1

Chapter 5

Conclusions

Vortex shedding suppression by different countermeasure mechanisms is a well-known study field. The helical-twisted profile is an alternative design of the cylinder, whose irregular cross-section can contribute to the reduction of the vortex shedding frequency.

A LES turbulence model is employed to investigate the vortex shedding of a circular cylinder. This pipe is further compared to five different configurations of helical-twisted pipes, with different groove's pitch and depth. Hence, an evaluation of the vortex shedding frequency reduction is carried out. In this document, a numerical model for the helical-twisted cylinder is proposed. The main conclusions of the project are summarized as follows:

- In helical-twisted profiles, the employment of less than a total of 1 million cells for the mesh is an insufficient approach for a LES model of vortex shedding. The usage of 1.6 million cells is considered to be enough to predict the phenomena. Although higher mesh resolutions are recommended, the computations can be extremely time consuming.

- The p/D = 1 e/D = 0.05 helical-twisted pipe effectively suppresses the vortex shedding frequency by 16%. In comparison to the circular cylinder, the magnitude of the lift coefficient is reduced, whereas variations in the drag coefficient are negligible.

- The twisted geometry of the p/D = 1 e/D = 0.05 profile appears to influence the vortex shedding by two mechanisms. The first one is the three-dimensional disturbance of the near wake, where lift coefficient fluctuationsseems to be counteracted, spanwise correlation. The average amplitude of this force was reduced by 8.53% comparing to the regular circular pipe. Regarding the second mechanism, the shape of the surface, with a sufficiently wide and deep groove, seems to help the flow to cross without significant accelerations. This reduces the disturbances in the near wake and eventually in the lift force fluctuation.

- It is found that "smoother" groove designs mitigate vortex shedding. This means that the variations on the surface given by the twisting procedure should be minimized, so the groove is not too deep or too wide. No significant correlation was found when varying the groove's depth or pitch.

- Certain helical-twisted configurations present mechanical advantages in the crossflow behavior which can potentially enhance the fluid-structure interaction and increase the lifespan of the structure, making it favorable for structural and mechanical purposes, which can be added to its safety properties for gripping.

Bibliography

[1] AcuRail. *Acurail Picture Gallery*. 2020. URL: `https://acurail.dk/en/gallery/`. (accessed: 15.02.2020).

[2] KAG Safety Rail. *KAG Grab Rails: Medical Range*. Brochure. 2020.

[3] R. D. Blevins and H. Saunders. *Flow-Induced Vibrations*. 2^{nd}. Van Nostrand Reinhold Co, 1990.

[4] M. Hayatdavoodi S. Rashidi and J.A. Esfahani. "Vortex Shedding Suppression and Wake Control: A Review". In: *Ocean Engineering* 126 (2016), pp. 57 –80.

[5] Jingyun Cheng Peimin Cao Mengmeng Zhang Shiwiao Fu Haokie Ren Yuwang Xu and Ziyang Zhu. "Vortex-induced Vibration of Flexible Pipe Fitted with Helical Strakes in Oscillatory Flow". In: *Ocean Engineering* 189 (2019).

[6] P. W. Bearman. "Circular cylinder wakes and vortex shedding". In: *Journal of Fluids and Structures* 27 (2011), pp. 648 –658.

[7] Zhaoyong Mao Wenlong Tian Tingying Zhang Peng Han Wei Wang Baowei Song. "Numerical investigation on vortex-induced vibration of bluff bodies with different rear edges". In: *Ocean Engineering* 197 (2020).

[8] L. Zou Y. Gao Z. Zong and Z. Jiang. "Effect of surface roughness on vortex-induced vibration response of a circular cylinder". In: *Ships and Offshore Structures* 13 (2018), pp. 28 –42.

[9] D. Lo Jacono J. Zhao J. Leontini and J. Sheridan. "The effect of mass ratio on the structural response of a freely vibrating square cylinder oriented at different angles of attack". In: *Journal of Fluid Mechanics* 86 (2019), pp. 200 –212.

[10] B. Seyed-Aghazadeh D. W. Carlson and Y. Modarres-Sadeghi. "Vortex-induced vibration and galloping of prisms with triangular cross-sections". In: *Journal of Fluid Mechanics* 817 (2017), pp. 590 –618.

[11] C. C. Feng. "The Measurement of Vortex Induced Effects in Flow Past Stationary and Oscillating Circular and D-Section Cylinders". PhD thesis. 1968.

[12] Mengmeng Zhang Shixiao Fu Yanxin Meng Haokie Ren Yuwan Xu and Chenyang Huang. "Distribution of Drag Coefficients Along a Flexible Pipe with Helical Strakes in Uniform Flow". In: *Ocean Engineering* 184 (2019), pp. 216 –226.

[13] R. Silvester. *Proceedings of the First Australasian Conference Held at the University of Western Australia, 6th to 13th December 1962*. 1^{st}. Pergamon, 1964. Chap. Flow over Immersed Bodies.

[14] M. M. Zdravkovich. “Review and Classification of Various Aerodynamic and Hydrodynamic Means for Suppressing Vortex Shedding”. In: *Journal of Wind Engineering and Industrial Aerodynamics* 7 (1981), pp. 145 –189.

[15] A. S. Sunil E. R. Ranjith and P. Lippin. “Analysis of Flow Over a Circular Cylinder Fitted with Helical Strakes”. In: *Procedia Technology* 24 (2016), pp. 452 –460.

[16] T. Ishibara and T. Li. “Numerical study on suppression of vortex-induced vibration of circular cylinder by helical wires”. In: *Journal of Wind Engineering & Industrial Aerodynamics* 197 (2020).

[17] S. Ganeshan and M. R. Rao. “Studies on thermohydraulics of single- and multi-start spirally corrugated tubes for water and time-independent power law fluids”. In: *International Journal of Heat and Mass Transfer* 25 (1982), pp. 1013 –1022.

[18] K. Sørensen J. Hærvig and T. J. Condra. “On the fully-developed heat transfer enhancing flow field in sinusoidally, spirally corrugated tubes using computational fluid dynamics”. In: *International Journal of Heat and Mass Transfer* 106 (2017), pp. 1051 –1062.

[19] C. H. K. Williamson. “The Existence of Two Stages in the Transition to Three-Dimensionality of a Cylinder Wake”. In: *Physics of Fluids* 31 (1988), pp. 3165 –3168.

[20] D. F. L Labbé and P. A. Wilson. “A Numerical Investigation of the Effects of the Spanwise Lenght on the 3-D Wake of a Circular Cylinder”. In: *Journal of Fluids and Structures* 23 (2007), pp. 1168 –1188.

[21] R. D. Henderson. “Nonlinear Dynamics and Pattern Formation in Turbulent Wake Transition”. In: *Journal of Fluid Mechanics* 352 (1997), pp. 65 –112.

[22] W. W. Huebsch B. R. Munson T. H. Okiishi and A. P. Rothmayer. *Fundamentals of Fluid Mechanics*. 7^{th}. John Wiley & Sons, Inc, 1977. Chap. Flow over Immersed Bodies.

[23] V. Strouhal. “Uber eine besondere Art der Tonerregung. Annalen der Physik und Chemie”. In: *Annalen der Physik und Chemie* 241(10) (1878), pp. 216 –251.

[24] C. H. K. Williamson and G. L. Brown. “A Series in $1/\sqrt{Re}$ to Represent the Strouhal-Reynolds Number Relationship of the Cylinder Wake”. In: *Journal of Fluids and Structures* 12 (1998), pp. 1073 –1085.

[25] A. Roshko. *On the Development of Turbulent Wakes from Vortex Streets*. 1954.

[26] H. Jiang and L. Cheng. “Strouhal-Reynolds Number Relationship for Flow Past a Circular Cylinder”. In: *Journal of Fluid Mechanics* 832 (2017), pp. 170 –188.

[27] M. König U. Fey and H. Eckelman. “A new Strouhal-Reynolds-Number Relationship for the Circular Cylinder in the Range”. In: *Physics of Fluids* 10 (1998), pp. 1547 –1549.

[28] A. Roshko. “On the Wake and Drag of Bluff Bodies”. In: *Journal of the Aeronautical Sciences* 22 (1955), pp. 124 –132.

[29] N. D. Katopodes. *Free-Surface Flow*. Butterworth-Heinemann, 2019.

[30] Ansys Inc. *Ansys Fluent Theory Guide Release 15.0*. SAS IP, 2013.

[31] M. Breuer and M. Münsch. “LES Meets FSI – Important Numerical and Modeling Aspects”. In: *Direct and Large-Eddy Simulation VII*. Ed. by B. Geurts V. Armenio and J. Fröhlich. Cost & Springer, 2010, pp. 245 –252.

[32] S. Heinz (Article in press). “A Review of Hybrid RANS-LES Methods for Turbulent Flows: Concepts and Applications”. In: *Progress in Aerospace Sciences* x (2020), p. x.

[33] B. Zamora C.G. Cutillas J. Ruiz A.S. Kaiser and M. Lucas. “CFD Analysis of Drift Eliminators Using RANS and LES Turbulent Models”. In: *Applied Thermal Engineering* 105 (2016), pp. 979 –987.

[34] H. Schlichting and K. Gersten. *Boundary Layer Theory*. 9^{th}. Springer, 1977.

[35] Danish Wind Industry Association. *Wind Map of Denmark*. 2020. URL: `http://xn--drmstrre-64ad.dk/wp-content/wind/miller/windpower\%20web/en/tour/wres/dkmap.htm`. (accessed: 15.02.2020).

[36] J. Smagorinsky. “General Circulation Experiments with the Primitive Equations. I. The Basic Experiment”. In: *Monthly Weather Review* 91 (1963), pp. 99 –164.

[37] H. T. Pham A. Van Dine and S. Sarkar. “Investigation of LES Models for a Stratified Shear Layer”. In: *Computers & Fluids* 198 (2020), pp. 104 –405.

[38] F. Nicoud and F. Ducros. “Subgrid-Scale Stress Modelling Based on the Square of the Velocity Gradient Tensor”. In: *Flow, Turbulence and Combustion* 62 (1999), pp. 183 –200.

[39] P. Domingo G. Lodato and L. Vervisch. “A WALE-Similarity Mixed Model for Large-Eddy Simulation of Wall Bounded Compressible Turbulent Flows”. In: *Direct and Large-Eddy Simulation VII*. Ed. by B. Geurts V. Armenio and J. Fröhlich. Cost & Springer, 2010, pp. 579 –586.

[40] M. V. Salvetti B-Koobus S. Wornom H. Ouvrard and A. Dervieux. “Variational Multiscale Large-Eddy Simulations of the Flow Past a Circular Cylinder: Reynolds Number Effects”. In: *Computer & Fluids* 47 (2011), pp. 44 –50.

[41] B. Pettersen M. A. Prsic M. C. Ong and D. Myrhaug. “Large Eddy Simulations of Flow Around a Smooth Circular Cylinder in a Uniform Current in the Subcritical Flow Regime”. In: *Ocean Engineering* 77 (2014), pp. 61 –73.

[42] S. Hickel X.Y. Hu M. Meyer A. Devesa and N.A. Adams. “An Immersed Interface Method in the Framework of Implicit Large-Eddy Simulation”. In: *Direct and Large-Eddy Simulation VII*. Ed. by B. Geurts V. Armenio and J. Fröhlich. Cost & Springer, 2010, pp. 122 –128.

[43] M. Laroussi and M. Djebbi. “Vortex Shedding for Flow Past Circular Cylinder: Effects of Initial Conditions”. In: *Universal Journal of Fluid Mechanics* 3 (2015), pp. 19 –32.

[44] The OpenFOAM Foundation. *OpenFOAM v7 User Guide*. 2020. URL: `https://cfd.direct/openfoam/user-guide`.

[45] C. H. K Williamson and A. Roshko. “Vortex Formation in the Wake of an Oscillating Cylinder”. In: *Journal of Fluids and Structures* 2 (1988), pp. 355 –381.

Appendices

Appendix A

NordBase Experimental Report

NordBase

NOTE

Date: 2020-mar-01
Init: FM
Mob +45 2345 4427
Mail. FM@nordbase.com

Hvirvelafløsning / Galloping

I gittertårne opbygget af cirkulære rørprofiler med høj slankhedstal er der risiko for hvirvelafløsning i de enkelte elementer. Ulempen udover ukontrollerede bevægelser er at risikoen for udmattelsesbrud grundet et højt svingningsantal ved især svejsesamlinger.

Hvirvelafløsning kan formelt eftervises ved

- DS/EN 1991-1-4 2. edt. 2017, Eurocode 1: Actions on structures, Part 1-4 General actions – Wind actions, Annex E alternativ
- Recommended Practice DNV-RP-C205 Environmental Conditions and Environmental Loads, April 2014. (giver erfaringsmæssig konservative resultater i forhold til Eurocode)

Profiler med relative lav aksial last er særlig udsat idet disse typisk udføres med høj slankhedstal. Dette gælder typisk

- Poles I top af mast udført som udkragede profiler benyttet enten som lynafleder, eller som understøting for mobilantenner
- Horisontaler, der benyttes som indvendig kryds i master med stor rodmål.
  Har her oplevet et eksempel på horizontal med dimension ø114mm, godstykkelse 8mm og længde 6412mm (egenfrekvens 16.9 Hz, L/i= 169.8) der kom i svingninger ved vindhastigheder ned til 5m/s.
  (en let hånd lagt på profilet var dog tilstrækkelig til at stoppe svingningerne)

Tårne udføres i dag gradvis højere og gradvis øget slankhedstal (Højde / rodmål). Der benyttes dimensioner hvor der erfaringsmæssig er et beskedent kendskab til deres opførsel – specielt mht til hvirvelafløsning / galloping. Specielt gælder at metrologiske tårne, udføres som fritstående 3-sidede gittertårne med højder op til 115m og rodmål 4.260m. Disse tårne har typiske horisontale udbøjninger i top på 2.90m for 20 års returvind.

Det vil være af særlig interesse om der kunne en etableres model for beregning af følsomheden for hvirvelafløsning af et sådant tårn og hvorvidt anvendelsen af et cirkulært rør med profilering i givet tilfælde kunne afhjælpe sådanne problematikker.

Med venlig hilsen
NordBase Engineering ApS

Finn Madsen

Finn Madsen

Appendix B

Mesh Convergence Test

B.1 Meshes For Circular Cylinder

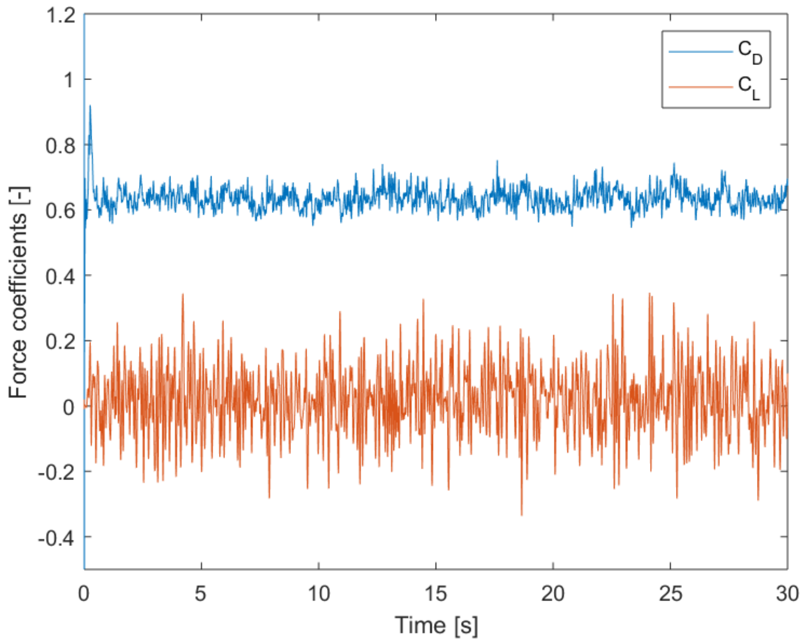

Figure B.1: **Aerodynamic force coefficients oscillation for mesh convergence test with 8 thousand cells**

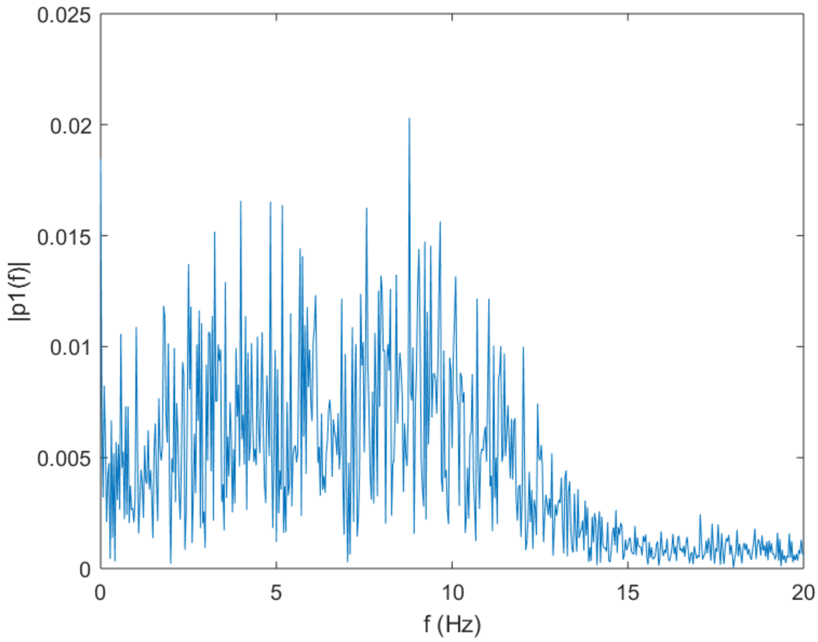

Figure B.2: **Power spectral density of the signal generated by the lift force coefficient in Mesh 1**

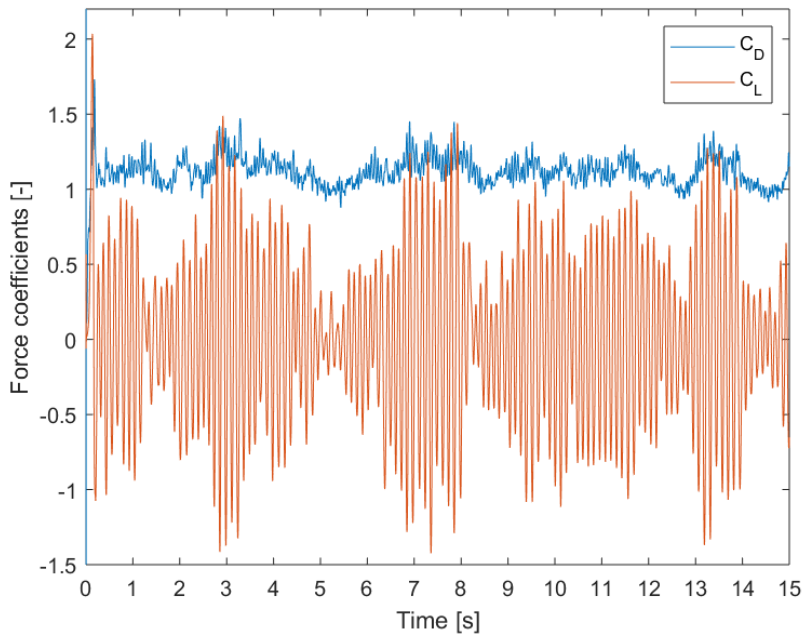

Figure B.3: **Aerodynamic force coefficients oscillation for mesh convergence test with 3.3 million cells**

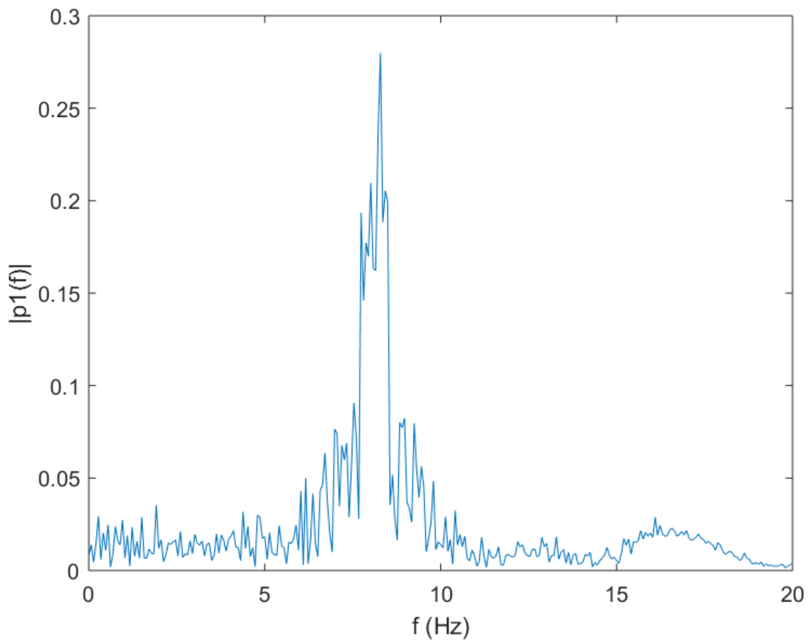

Figure B.4: **Power spectral density of the signal generated by the lift force coefficient in Mesh 3**

B.2 Meshes For Helical-twisted Cylinder With p/D = 1 And e/D = 0.1

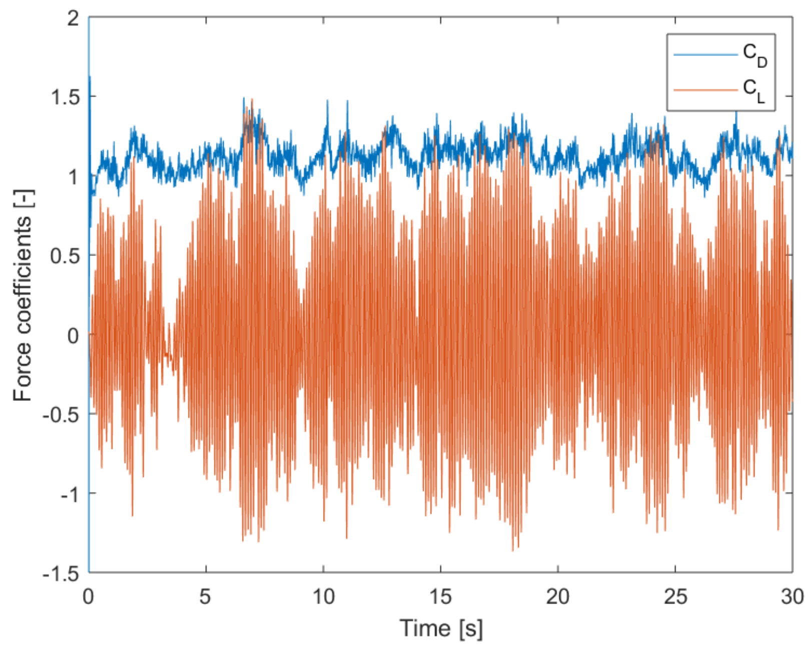

Figure B.5: **Aerodynamic force coefficients oscillation for mesh convergence test with 8 thousand cells**

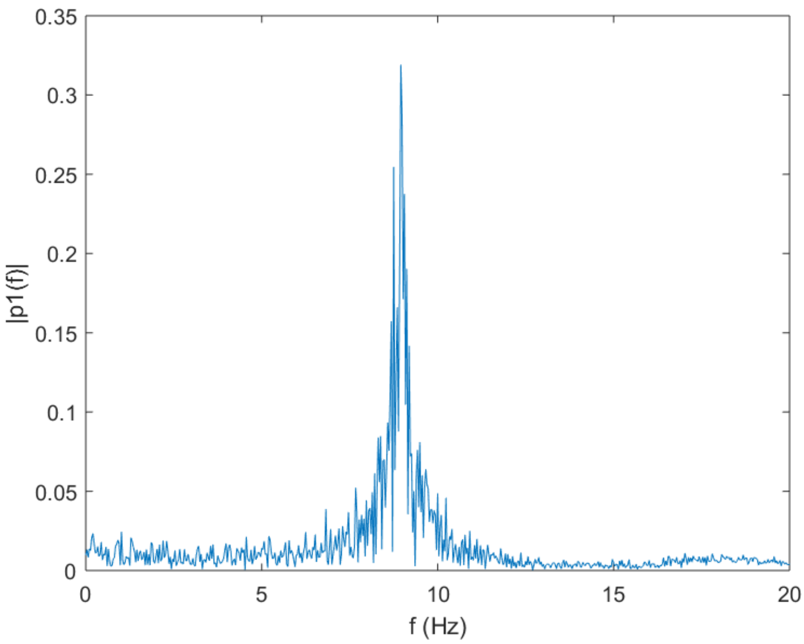

Figure B.6: **Power spectral density of the signal generated by the lift force coefficient in Mesh 1**

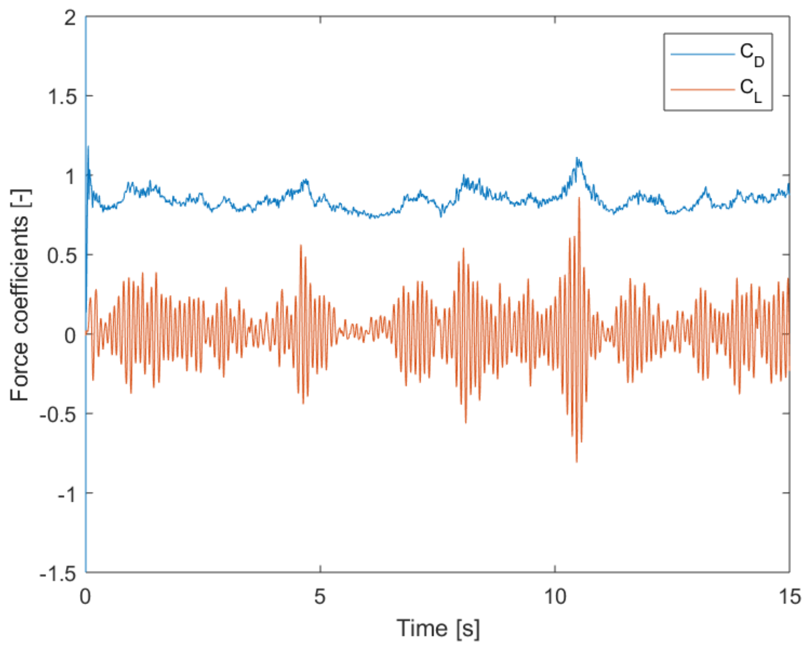

Figure B.7: **Aerodynamic force coefficients oscillation for mesh convergence test with 3.3 million cells**

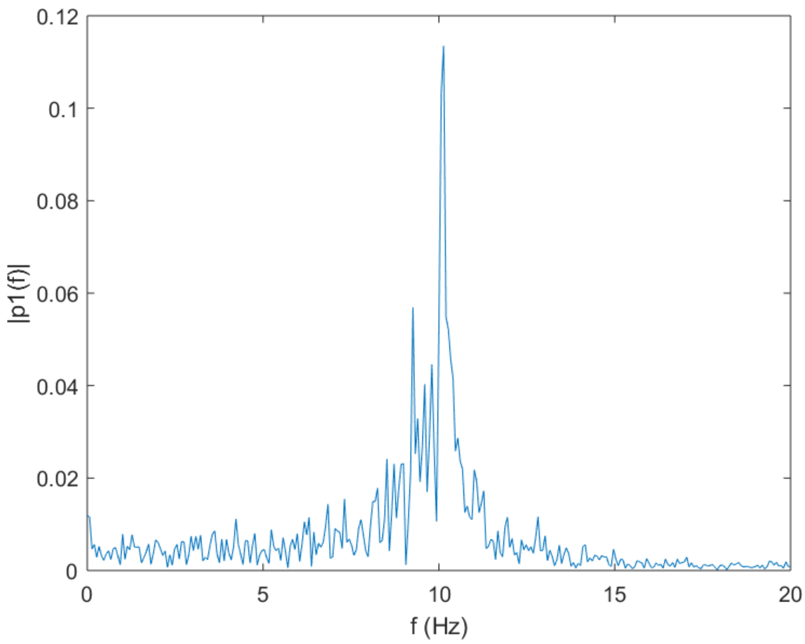

Figure B.8: **Power spectral density of the signal generated by the lift force coefficient in Mesh 3**

Appendix C

MatLab Code For Fast Fourier Transformation (FFT)

The FFT was used to extract the vortex shedding frequency for each cylinder case.

%% Reading the table from "forceCoeffs.dat" output file from OpenFOAM

» table = readtable('forceCoeffs.dat');
» Cl = table(:,4); t = table(:,1);

% Getting the array

» Cl = table2array(Cl);Cl=Cl'
» t = table2array(t);t=t'

%% Erasing unstable/diverging results from the first 400 samples

» for i = 1:400
» Cl(i) = [];
» end

%% FFT for frequency analysis

» Ts = mean(diff(t)); % Getting the time step of the simulation
» Fs = 1/Ts; % Sampling frequency
» L = length(Cl); % Length of signal
» xdft = fft(Cl); % Computing the FFT of the signal

% For computing the two-sided spectrum p2, then the single-sided p1 based on p2
% and the even-valued signal length L

» p2 = abs (xdft)/L;
» p1 = p2(1:L/2+1);
» p1(2:end-1) = 2* p1(2:end-1);

% Defining the frequency domain f

» fv = 0:Fs/L:Fs/2;

% Plotting the single-sided amplitude spectrum p1 against f domain

» figure
» plot(fv,p1)
» xlabel('f (Hz)');
» xlim([0 20]);
» ylabel('|p1(f)|');

Appendix D

Other Plots Of Results

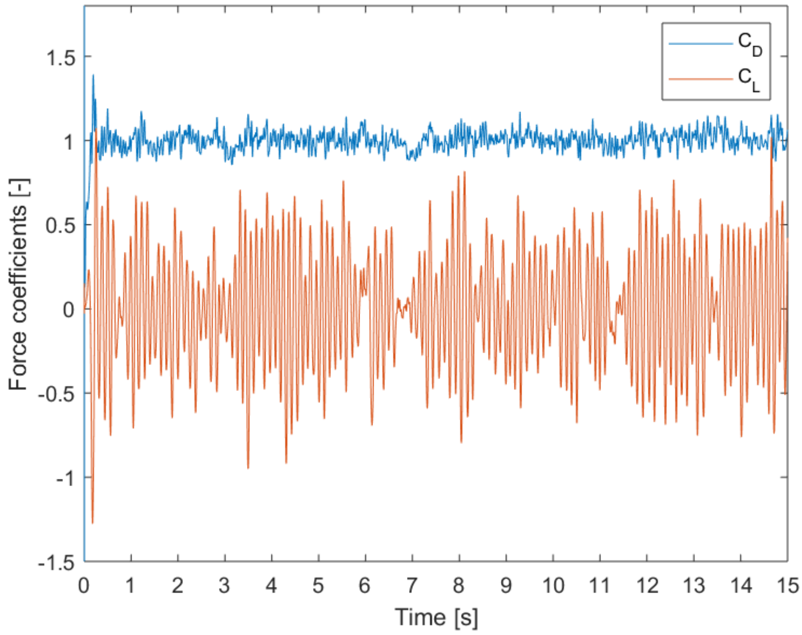

Figure D.1: **Sampling of drag and lift force coefficients in the circular cylinder at Re = $3.7{\cdot}10^4$, with a 1.6 million cells**

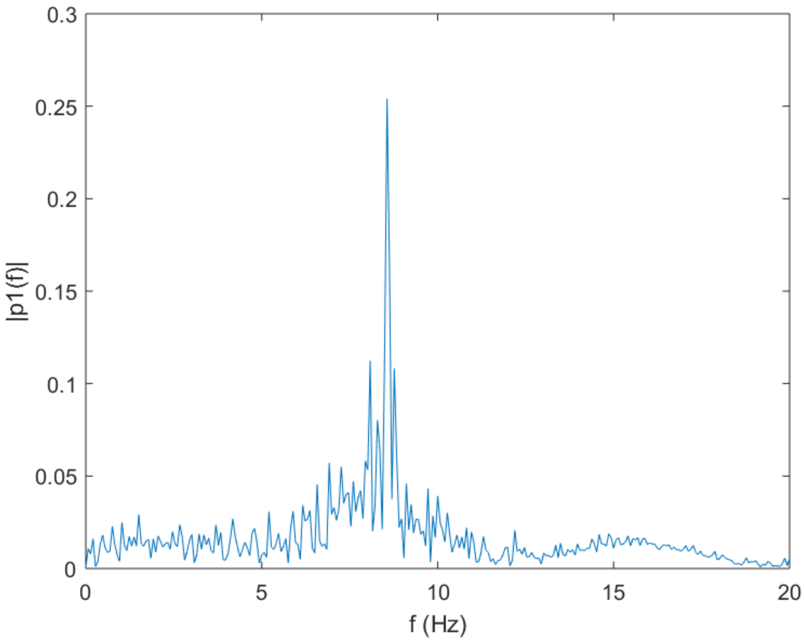

Figure D.2: **Single-Sided Amplitude Spectrum. Signal's PSD generated by the lift force coefficient with a Mesh of 1.6 million cells for circular cylinder at Re = $3.7{\cdot}10^4$**

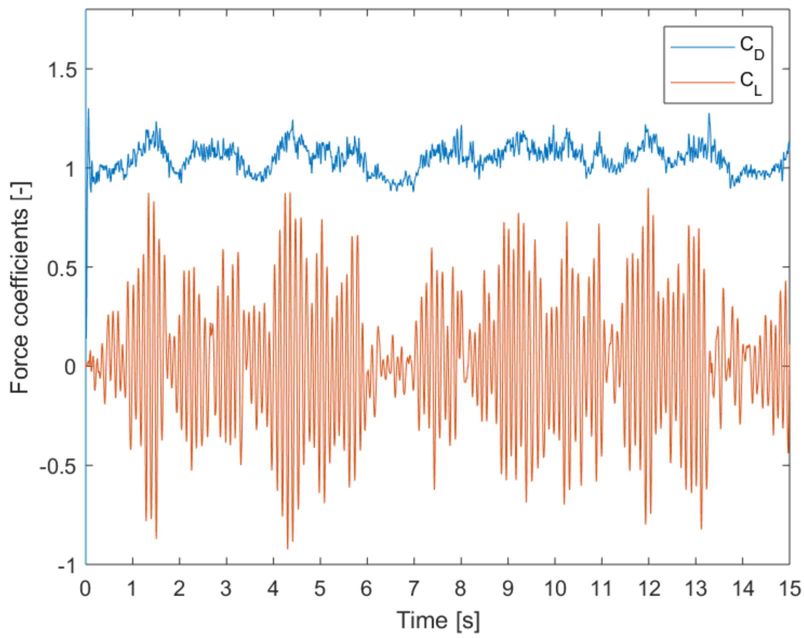

Figure D.3: **Aerodynamic force coefficients of helical twisted p/D = 1 e/D = 0.05**

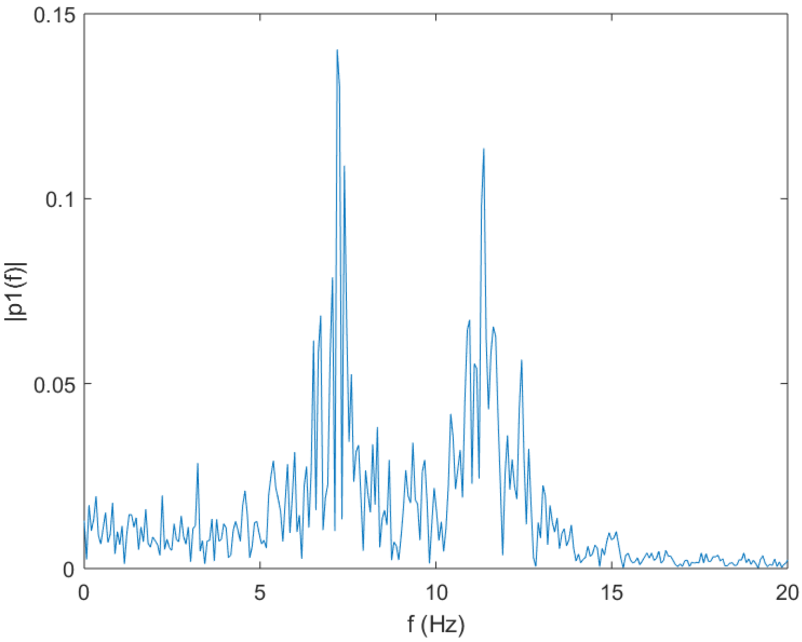

Figure D.4: **PSD from helical twisted p/D = 1 e/D = 0.05**

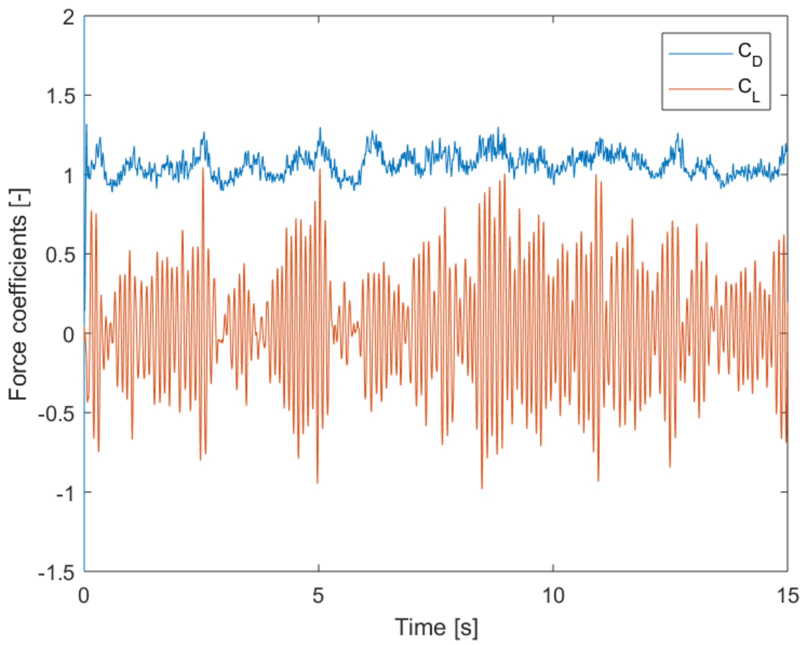

Figure D.5: **Sampling of drag and lift force coefficients in the helical-twisted cylinder p/D = 1 and e/D = 0.1, with a 1.6 million cells**

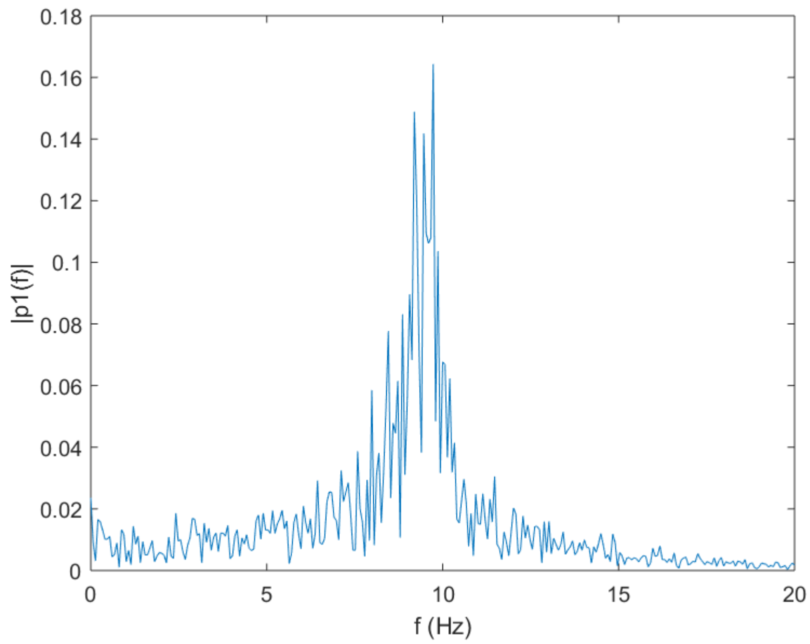

Figure D.6: **Single-Sided Amplitude Spectrum. Signal's PSD generated by the lift force coefficient with a Mesh of 1.6 million cells for the helical-twisted cylinder p/D = 1 and e/D = 0.1**

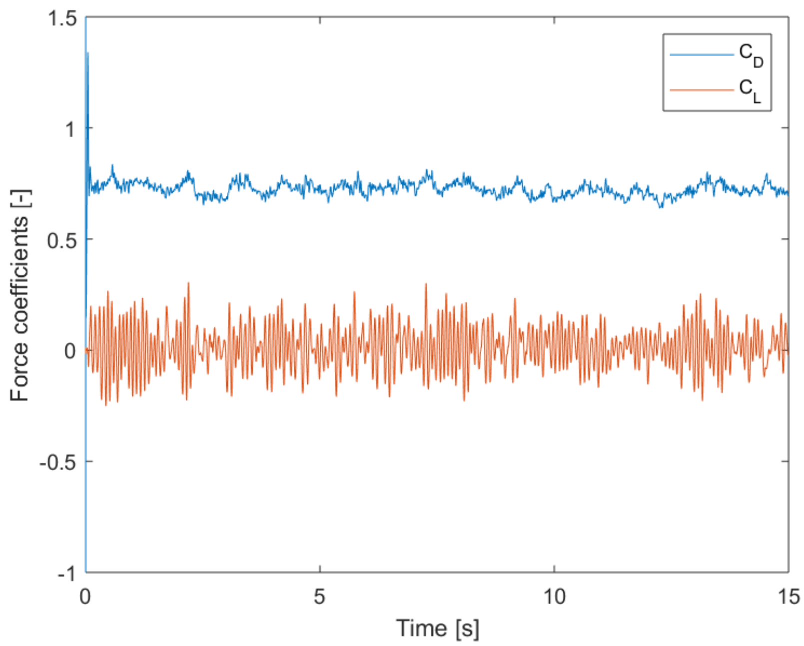

Figure D.7: **Aerodynamic force coefficients of helical twisted p/D = 1 e/D = 0.2**

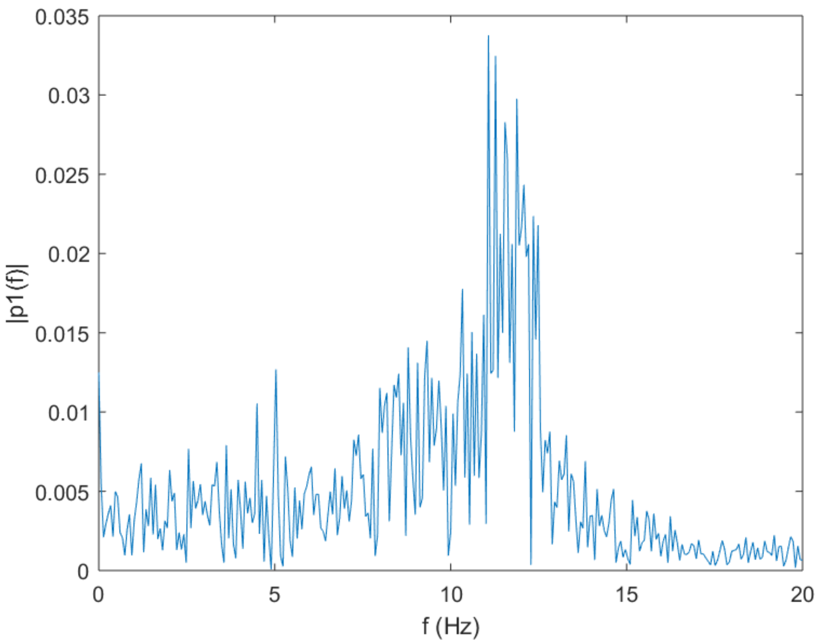

Figure D.8: **PSD from helical twisted p/D = 1 e/D = 0.2**

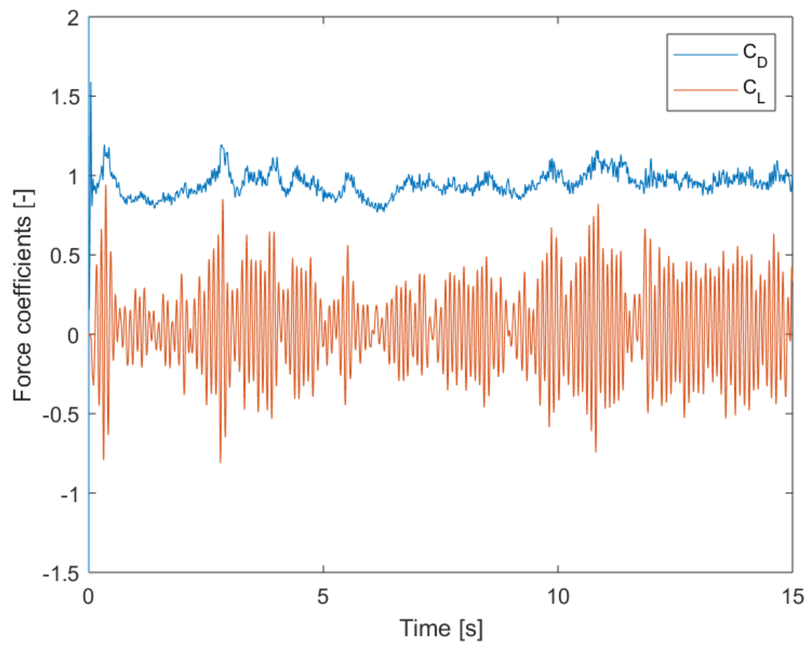

Figure D.9: **Aerodynamic force coefficients of helical twisted p/D = 0.5 e/D = 0.1**

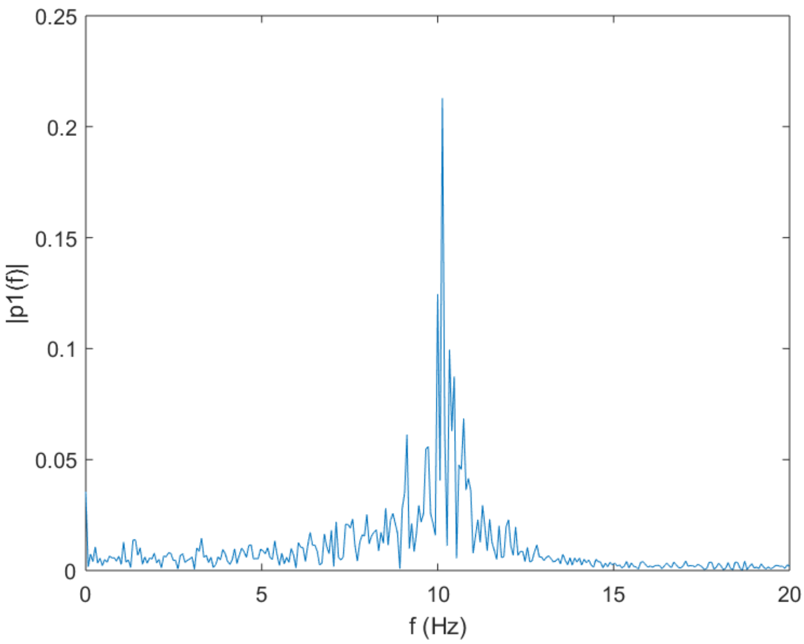

Figure D.10: **PSD from helical twisted p/D = 0.5 e/D = 0.1**

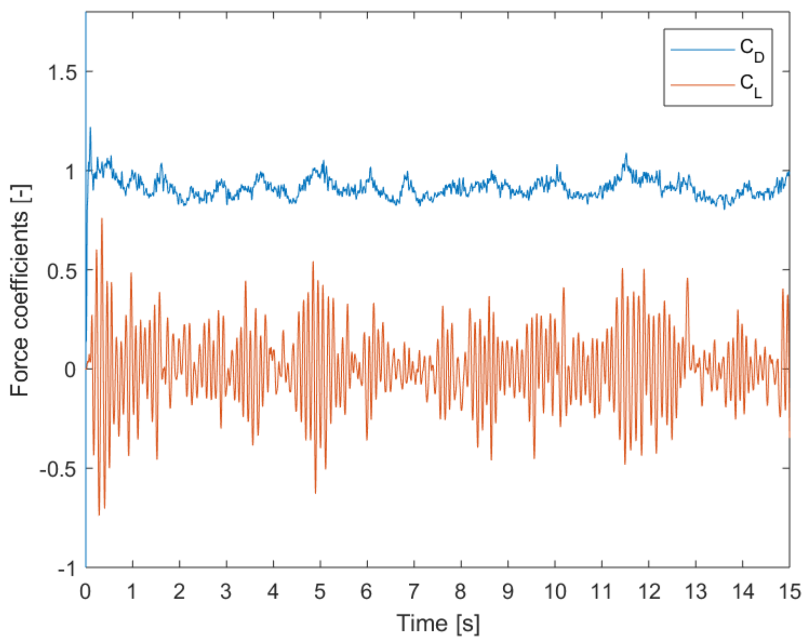

Figure D.11: **Aerodynamic force coefficients of helical twisted p/D = 2 e/D = 0.1**

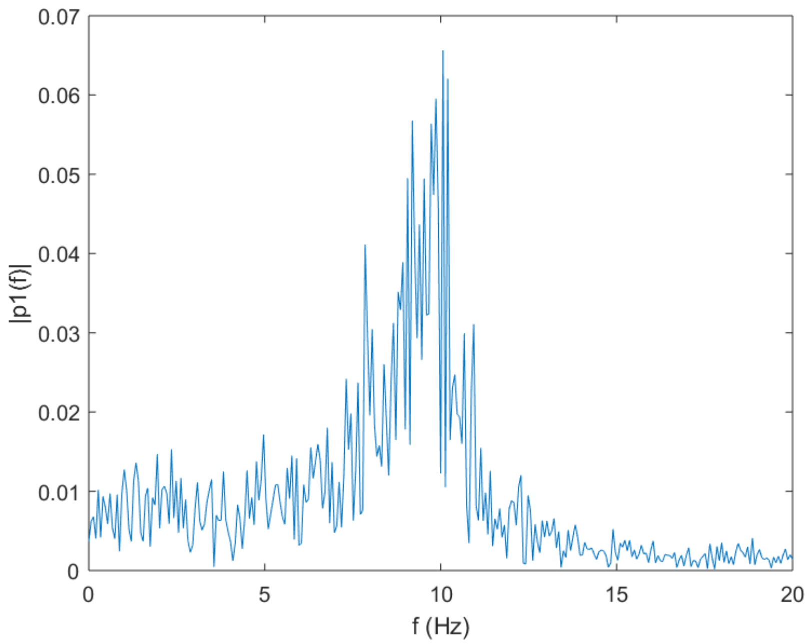

Figure D.12: **PSD from helical twisted p/D = 2 e/D = 0.1**

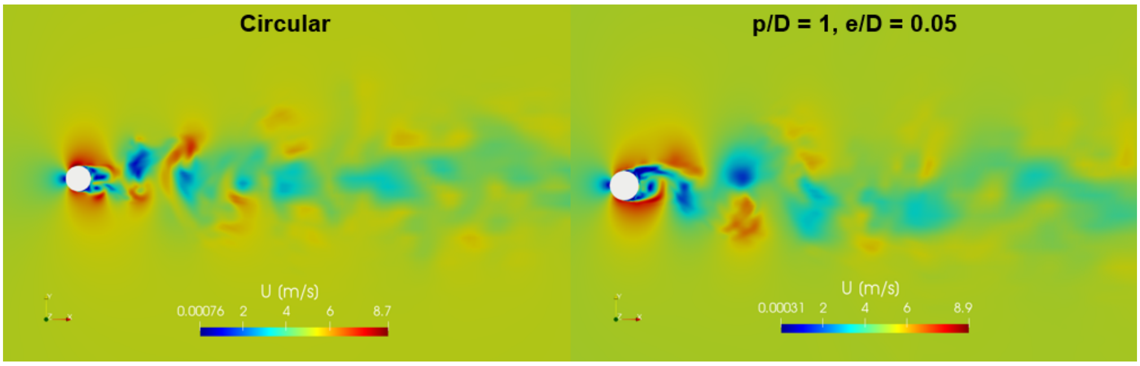

Figure D.13: **Zoom detail of the circular and p/D = 1 e/D = 0.05 helical-twisted cylinders**